Check for updates



NEUROSCIENCE

# Astrocyte redox imbalance underlies prelimbic neuronal hypoactivity and maladaptive affective behaviors in epilepsy

**Travis E. Faust[1]†, Atsushi Saito[2], Shoichi Ishikawa[1], Kun Yang[3], Wendy Xin[1,4]‡, Ho Namkung[5], Amit Agarwal[1,6], Adriana Ramos[3]§, Brian J. Lee[3]¶, Lindsay Hayes[1], Rupali Srivastava[3], Sunday Adelakun[3], Sneha Saha[3], Trexy Palen[3], Tyler Cash-Padgett[3], Daniel J. Wood[3], Elisa Carloni[3], Ryosuke Yusa[3]#, Hanna Jaaro-Peled[3], Jed W. Fahey[2,3,7,8], Dwight E. Bergles[1,9], Koko Ishizuka[3], Akira Sawa[1,2,3,5,10,11]***

Copyright © 2026 The Authors, some rights reserved; exclusive licensee American Association for the Advancement of Science. No claim to original U.S. Government Works. Distributed under a Creative Commons Attribution License 4.0 (CC BY).

**A fundamental but unanswered question in neuropsychiatry is whether the psychiatric symptoms of epilepsy are caused by the same or a separate pathophysiology as seizures. To address this question, we investigated a monogenic form of epilepsy (pyridoxine-dependent epilepsy) caused by aldehyde dehydrogenase 7 family member A1 (ALDH7A1) mutations. ALDH7A1 global knockout mice exhibited both seizure-associated and maladaptive affective behavioral phenotypes. However, seizure phenotypes were caused by ALDH7A1 deletion in hepatocytes whereas maladaptive affective behaviors were caused by ALDH7A1 deletion in astrocytes. Deletion in astrocytes disrupted astrocyte redox homeostasis, impairing regulation of extracellular ion concentrations and reducing neuronal activity in the prelimbic cortex. Sulforaphane, which activates the NRF2 antioxidant pathway, restored prelimbic neuronal activity and rescued maladaptive affective behaviors in ALDH7A1 knockout mice but did not prevent seizures. These studies implicate astrocyte redox homeostasis and prelimbic hypoactivity in maladaptive affective behavioral phenotypes in a congenital form of epilepsy, which are mechanistically and therapeutically dissociable from seizure pathophysiology.**

## INTRODUCTION

Patients diagnosed with epilepsy suffer not only from seizures but also from psychiatric and cognitive symptoms in the periods between seizures (*1*, *2*). A fundamental but unanswered question is whether psychiatric and cognitive symptoms in epilepsy stem from the same pathophysiology that causes seizures or a separate pathophysiology (*3*). Epidemiological and genetic studies suggest that etiological factors are at least in part shared between epilepsy and major psychiatric disorders (*4*–*6*), but there is a lack of neurobiological studies on psychiatric symptoms in epilepsy to address this question. Resolving this mechanistic ambiguity will provide guidance for future treatment of psychiatric symptoms associated with epilepsy and further inform treatment of psychiatric disorders in general.

Many sporadic neuropsychiatric disorders such as epilepsy are clinically defined, which results in diagnoses that are etiologically and pathophysiologically heterogeneous. Accordingly, scientists have increasingly turned to rare genetic disorders in which the biological mechanisms can be logically studied from a single genetic etiology to clinical manifestations, which, in turn, provides invaluable insight to sporadic conditions (*7*). One such case is pyridoxine-dependent epilepsy (PDE), which is caused in humans by loss-of-function mutations in the aldehyde dehydrogenase 7 family member A1 (ALDH7A1) gene (*8*). PDE is a good model for understanding the pathophysiology of psychiatric symptoms in epilepsy because seizures in PDE are responsive to high doses of pyridoxine (also known as vitamin B6), yet psychiatric symptoms are nonresponsive to pyridoxine and persist into adulthood even after seizures are controlled (*9*, *10*). Furthermore, the astrocyte-specific expression pattern of *ALDH7A1* in the mature brain (*11*) facilitates molecular dissection of its cellular mechanism using genetic tools in animal models.

Astrocytes are principally responsible for homeostatic functions to support other brain cells, particularly neurons (*12*). In addition to metabolic functions, astrocytes influence neuronal activity through regulation of synaptogenesis, synaptic strength, neuronal excitability, and extracellular levels of ions and neurotransmitters (*13*, *14*). Aldehyde dehydrogenase (ALDH) family genes have enriched expression in astrocytes (*11*), but the biological consequences of this restricted ALDH expression pattern remain unexplored. Enzymatically, ALDHs oxidize a wide range of endogenous and exogenous aldehydes into

[1]Department of Neuroscience, Johns Hopkins University School of Medicine, Baltimore, MD 21205, USA. [2]Department of Physiology, Pharmacology, and Therapeutics, Johns Hopkins University School of Medicine, Baltimore, MD 21205, USA. [3]Department of Psychiatry, Johns Hopkins University School of Medicine, Baltimore, MD 21205, USA. [4]Synaptic Plasticity Section, Cellular Neurobiology Branch, National Institute on Drug Abuse Intramural Research Program, Baltimore, MD 21224, USA. [5]Department of Biomedical Engineering, Johns Hopkins University School of Medicine, Baltimore, MD 21205, USA. [6]The Chica and Heinz Schaller Research Group, Institute for Anatomy and Cell Biology, Heidelberg University, 69120 Heidelberg, Germany. [7]Department of Medicine, Johns Hopkins University School of Medicine, Baltimore, MD 21205, USA. [8]Institute of Medicine, University of Maine, Orono, ME 04469, USA. [9]Johns Hopkins University Kavli Neuroscience Discovery Institute, Baltimore, MD 21205, USA. [10]Department of Genetic Medicine, Johns Hopkins University School of Medicine, Baltimore, MD 21205, USA. [11]Department of Mental Health, Johns Hopkins Bloomberg School of Public Health, Baltimore, MD 21205, USA.
*Corresponding author. Email: asawa1@jhmi.edu
†Present address: Department of Neurobiology, Brudnick Neuropsychiatric Research Institute, University of Massachusetts Chan Medical School, Worcester, MA 01605, USA.
‡Present address: Donald K. Johnson Eye Institute and Krembil Brain Institute, University Health Network, Department of Physiology, University of Toronto, Toronto, ON M5T 0S8, Canada.
§Present address: Neurology Therapeutic Area, Sanofi, Cambridge, MA 02142, USA.
¶Present address: Department of Psychiatry, Indiana University School of Medicine, Indianapolis, IN 46202, USA.
#Present address: Department of Immunology, Graduate School of Medicine and Faculty of Medicine, The University of Tokyo, Tokyo 113-0033, Japan.

Downloaded from https://www.science.org on August 04, 2026

carboxylic acids via NAD(P)$^+$-dependent reactions (*15*) with overlapping substrate specificities (*16*). As producers of NAD(P)H, ALDHs affect cellular redox homeostasis (*17*–*20*), which, in turn, influences other redox-dependent cellular activities. In many tissues and organisms, efficient aldehyde degradation by ALDHs is needed to limit toxic, electrophilic reactions between aldehydes and cellular macromolecules (*21*–*23*) and protect against massive oxidative stress (*24*, *25*). The brain's exposure to aldehydes may be especially high due to its high concentration of lipids and large energy demands (*26*). Although initial efforts of characterizing basic function of ALDH7A1 through loss-of-function models are just emerging (*27*–*30*), it remains elusive how ALDH7A1 influences astrocyte-neuron interactions and behavior.

The major psychiatric symptoms in patients with epilepsy include mood-associated manifestations, which affect more than one-third of the patients (*1*, *31*) including those with PDE (*32*). The current diagnosis of mood disorders includes a heterogeneous set of disease conditions in which the involvement of oxidative stress and inflammatory processes (*33*, *34*), alterations of neuronal connectivity (*35*), and dysfunction of astrocytes (*36*) have all been reported. Several assays have been developed to assess maladaptive affective behaviors in rodents likely to be relevant to human mood disorders including the forced swim test (FST), a measure of passive coping behavior (*37*), and the sucrose splash test, a measure of self-care and motivational behavior (*38*). These assays have proven useful for drug discovery and for investigating neural circuitry relevant to mood disorders (*39*–*41*). In one well-described circuit, maladaptive affective behavior in rodents is reversibly controlled by the activity of pyramidal neurons in layer 5 (L5) of the prelimbic cortex (*42*), making this a useful circuit to connect behavioral symptoms with cellular/molecular mechanisms underlying mood disorders.

In the present study, we generated a mouse model of PDE with constitutive global depletion of ALDH7A1 (KO$^{Global}$) that exhibited increased seizure susceptibility and maladaptive affective behaviors. On the basis of the expression pattern of ALDH7A1, we also generated astrocyte-specific (cKO$^{Astro}$) and liver-specific (cKO$^{Liver}$) ALDH7A1 conditional knockout (KO) mice that each showed only a partial phenotype: cKO$^{Astro}$ mice had maladaptive affective behaviors without any increase in seizure susceptibility, whereas cKO$^{Liver}$ mice had increased seizure susceptibility without maladaptive affective behavior. To understand how astrocytic disruption of ALDH7A1 gives rise to maladaptive affective behaviors, but not seizure phenotypes, we performed RNA sequencing (RNA-seq) and identified changes in astrocyte redox homeostasis in ALDH7A1-deficient astrocytes, which we further validated by biochemistry and imaging approaches. Treating mice with dietary sulforaphane (SFN), which augmented NRF2 signaling in astrocytes, ameliorated maladaptive affective behaviors in cKO$^{Astro}$ and KO$^{Global}$ mice, supporting the importanceof astrocyte redox homeostasis in maladaptive affective behaviors. Both dietary SFN and astrocyte-specific activation of the NRF2 pathway also ameliorated the reductions in L5 pyramidal neuron activity observed in the prelimbic cortex in cKO$^{Astro}$ and KO$^{Global}$ mice, which may contribute to these maladaptive affective behaviors. Pharmacological, electrophysiological, and additional transcriptomic experiments suggest that astrocyte redox imbalance causes this neuronal hypoactivity by impairing astrocyte regulation of extracellular ion concentrations. Together, these data indicate an astrocyte-driven mechanism of maladaptive affective behavioral phenotypes in PDE that is dissociable from seizures. These findings may further apply to more general cases of major depressive disorder (MDD) in which both astrocyte dysfunction and redox imbalance can occur (*34*, *36*).

## RESULTS

### Astrocyte ALDH7A1 contributes to maladaptive affective behaviors but not seizure susceptibility

We first generated mice with constitutive global deletion of *Aldh7a1* in all tissues (KO$^{Global}$) to serve as a mouse model of PDE (Fig. 1, A and B). We validated the deletion of *Aldh7a1* in KO$^{Global}$ mice by polymerase chain reaction (PCR) (fig. S1A), and loss of ALDH7A1 protein expression by immunohistochemistry (Fig. 1, C and D, and fig. S1B) and Western blotting (Fig. 1E). KO$^{Global}$ mice were viable, maintained a normal life span at least into adulthood, and exhibited no differences in weight (fig. S1C) or locomotion (fig. S1D). Mimicking the epileptic phenotype observed in patients with PDE, KO$^{Global}$ mice exhibited increased sensitivity to the chemoconvulsant pentylenetetrazol (PTZ) (Fig. 1F), which was rescued by dietary treatment with pyridoxine (fig. S1E), the compound used to ameliorate seizures in patients with PDE. KO$^{Global}$ mice also displayed reduced responses in two rodent tests of maladaptive affective behavior: the FST (Fig. 1G) and the sucrose splash test (Fig. 1H). Thus, KO$^{Global}$ mice model key aspects of PDE, including both seizure susceptibility and maladaptive affective behaviors.

We next examined the cellular expression pattern of ALDH7A1, using KO$^{Global}$ mice as the negative control. ALDH7A1 was expressed in astrocytes throughout the brain but not in other major brain cell types (fig. S2, A to J). ALDH7A1 expression was also higher in adult mice compared to weanlings (fig. S2, K and L) but did not differ between males and females (fig. S2, M and N). Outside the brain, ALDH7A1 was expressed in the kidney and liver (fig. S1B) but not in other tissues. On the basis of the expression profile of ALDH7A1, we decided to generate mice with conditional deletion of *Aldh7a1* in astrocytes (cKO$^{Astro}$ mice) using *Slc1a3*$^{CreER}$ and mice with conditional deletion of *Aldh7a1* in the liver (cKO$^{Liver}$ mice) using *Alb1*$^{Cre}$ (Fig. 1B). Immunohistochemical assessment (Fig. 1, I and J) and Western blotting (Fig. 1K) confirmed that ALDH7A1 was efficiently depleted from astrocytes in cKO$^{Astro}$ mice (~90% in the cortex and 50% in the rest of the brain) and maintained in peripheral organs (fig. S1B). In cKO$^{Liver}$ mice, ALDH7A1 was efficiently depleted from the liver (fig. S1B) and was maintained within the brain (Fig. 1, I and J).

Comparing the behavior of cKO$^{Astro}$ mice to KO$^{Global}$ mice, we paradoxically observed a higher seizure threshold (i.e., a lower seizure susceptibility) in cKO$^{Astro}$ mice compared to Cre-negative littermate controls (Con$^{Astro}$) (Fig. 1L), opposite to the effect observed in KO$^{Global}$ mice. To confirm this result, we also assessed seizure threshold in mice with constitutive, embryonic deletion of *Aldh7a1* in all forebrain astrocytes and neurons (*Emx1*$^{Cre/+}$; *Aldh7a1*$^{flox/flox}$ mice) (*43*) and again found a higher seizure threshold (fig. S1F). These results suggested that depletion of ALDH7A1 from forebrain astrocytes does not drive the increased seizure susceptibility observed in KO$^{Global}$ mice. However, despite the lack of seizure susceptibility, cKO$^{Astro}$ mice still phenocopied the maladaptive affective behaviors of KO$^{Global}$ mice with reduced mobility in the FST (Fig. 1M) and reduced grooming frequency and increased grooming latency during the sucrose splash test (Fig. 1N). These results suggest that astrocytes contribute to the maladaptive affective behaviors in KO$^{Global}$ mice but not the increased seizure susceptibility.

Downloaded from https://www.science.org on August 04, 2026

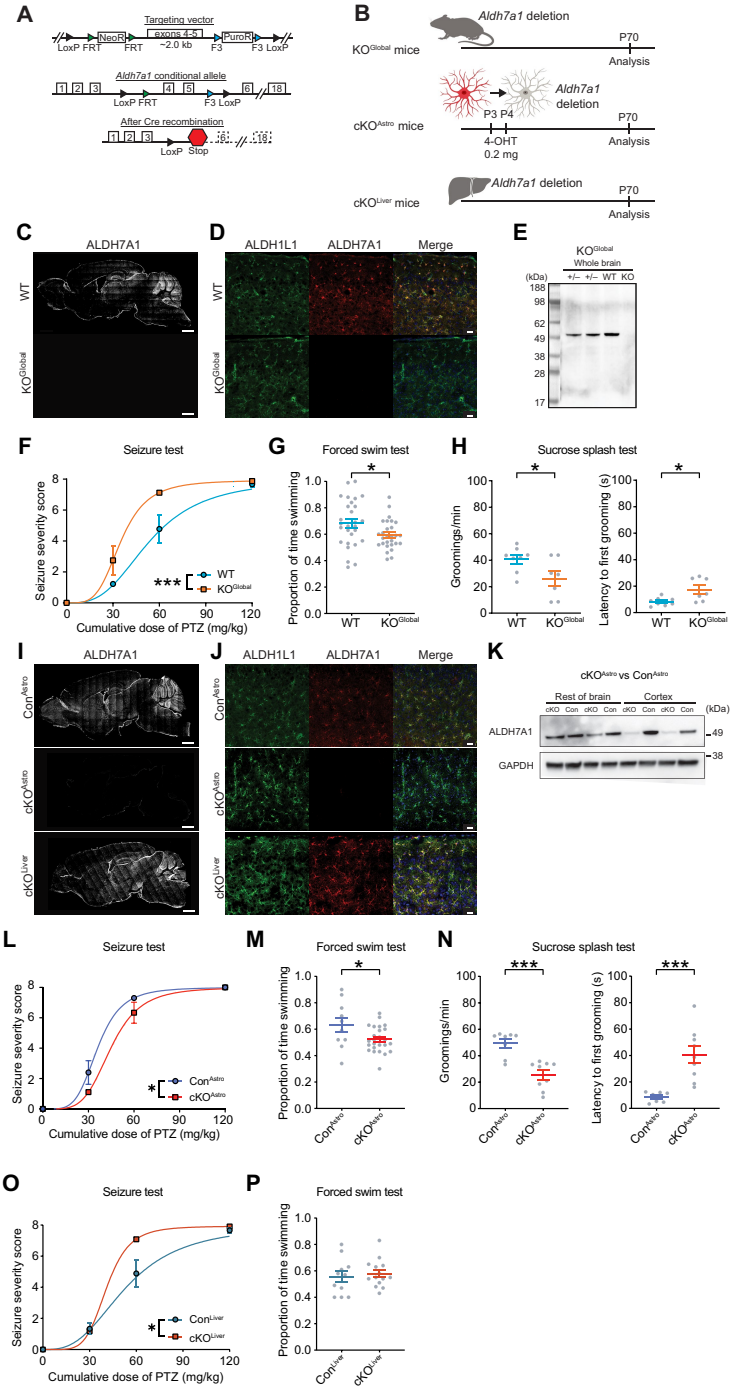


**Fig. 1. Astrocyte ALDH7A1 contributes to maladaptive affective behaviors but not the seizure susceptibility caused by ALDH7A1 dysfunction in the liver.** (**A**) Generation of floxed *Aldh7a1* mice (top) and recombination of the floxed allele (bottom). (**B**) Generation of KO$^{Global}$, cKO$^{Astro}$, and cKO$^{Liver}$ mice. (**C** and **D**) Representative ALDH7A1 immunofluorescence in sagittal brain sections (C; scale bars, 1000 μm) and cortex (D; scale bars, 20 μm) from KO$^{Global}$ and WT mice, colabeled for ALDH1L1. (**E**) Western blotting of ALDH7A1 in brain tissue from KO$^{Global}$ (KO), heterozygous (+/−), and WT mice. (**F**) PTZ seizure threshold test in KO$^{Global}$ and WT mice. Lines indicate fitted dose-response curves ($n = 8$ to 9 mice; ***$P < 0.001$). (**G**) FST: time swimming in KO$^{Global}$ and WT mice ($n = 28$ mice; *$P < 0.05$). (**H**) Sucrose splash test: grooming frequency and latency to grooming in KO$^{Global}$ and WT mice ($n = 7$ to 8 mice; *$P < 0.05$). (**I** and **J**) Representative ALDH7A1 immunofluorescence in sagittal sections (I; scale bars, 1000 μm) and cortex (J; scale bars, 20 μm) of cKO$^{Astro}$, Con$^{Astro}$, and cKO$^{Liver}$ mice, colabeled with ALDH1L1. (**K**) Western blotting of ALDH7A1 and GAPDH in the cortex and rest-of-brain homogenates from cKO$^{Astro}$ and Con$^{Astro}$ mice. (**L**) PTZ seizure threshold test in cKO$^{Astro}$ and Con$^{Astro}$ mice. Lines indicate fitted dose-response curves ($n = 9$ to 10 mice; *$P < 0.05$). (**M**) FST: time swimming in cKO$^{Astro}$ and Con$^{Astro}$ mice ($n = 10$ to 25 mice; *$P < 0.05$). (**N**) Sucrose splash test: grooming frequency and latency to grooming in cKO$^{Astro}$ and Con$^{Astro}$ mice ($n = 8$ to 9 mice; ***$P < 0.001$). (**O**) PTZ seizure threshold test in cKO$^{Liver}$ and Con$^{Liver}$ mice. Lines indicate fitted dose-response curves ($n = 9$ to 11 mice; *$P < 0.05$). (**P**) FST: time swimming in cKO$^{Liver}$ and Con$^{Liver}$ mice ($n = 11$ to 14 mice; $P > 0.05$). Data represent means ± SEM. Statistics: Extra sum-of-squares *F* test on $EC_{50}$ [(F), (L), and (O)]; Student's *t* test [(G), (H), (M), (N), and (P)]. Graphic elements created in BioRender. Faust, T. (2026) https://BioRender.com/owukrj6.

Downloaded from https://www.science.org on August 04, 2026

In contrast to cKO$^{Astro}$ mice, cKO$^{Liver}$ mice had a lower seizure threshold (i.e., higher seizure susceptibility) compared to Con$^{Liver}$ mice, phenocopying the result observed in KO$^{Global}$ mice (Fig. 1O). However, cKO$^{Liver}$ mice did not show any significant difference in mobility during the FST (Fig. 1P). These data suggest that ALDH7A1 depletion in the liver, rather than in astrocytes, drives the increase in seizure susceptibility in KO$^{Global}$ mice and that ALDH7A1 depletion in astrocytes, but not the liver, is responsible for the maladaptive affective behaviors in KO$^{Global}$ mice.

### Astrocyte ALDH7A1 regulates cellular redox homeostasis

In patients with PDE, seizures can be controlled by pyridoxine, but psychiatric symptoms remain intractable. We therefore focused on determining how ALDH7A1 depletion in astrocytes drives maladaptive affective behaviors. Although several functions of ALDH7A1 have been described in other tissues (*19*, *44*), the function of ALDH7A1 in the brain has not been determined. To investigate how ALDH7A1 depletion leads to brain dysfunction, we first performed RNA-seq on brain tissue homogenate from KO$^{Global}$ mice (Fig. 2A), focusing on the cortex where ALDH7A1 depletion was most robust in cKO$^{Astro}$ mice (Fig. 1, J and K). As expected, *Aldh7a1* expression was significantly decreased in the brain of KO$^{Global}$ mice, but only three other genes (*Hist1h1c*, *Prelp*, and *Hist1h1e*) reached gene-level significance (adjusted $P < 0.05$; Fig. 2B and table S1), suggesting that the brain transcriptome is largely unaltered by ALDH7A1 depletion. Nevertheless, gene set enrichment analysis (GSEA) of all detected genes identified 338 affected pathways (table S1), which we clustered into 38 biological themes using EnrichmentMap (*45*) (Fig. 2C). Although most PDE research has focused on the role of ALDH7A1 in lysine degradation (*8*, *46*), a majority of the themes that were down-regulated in KO$^{Global}$ brains were related to cellular redox processes (e.g., NADH dehydrogenase activity, glutathione (GSH) binding, cellular respiration, and lipid catabolism). To validate these findings, we performed biochemical assays to assess cellular redox status in tissue homogenate from KO$^{Global}$ mice. Compared to wild-type (WT) littermates, KO$^{Global}$ mice had a lower NAD$^+$/NADH ratio in cortical tissue homogenates (Fig. 2, D and E). For the NADP$^+$/NAPDH ratio and GSH/GSSG ratio, we further restricted our analysis to the prelimbic cortex (Fig. 2F), a region of the cortex known to regulate maladaptive affective behavior during the FST (*42*), and found no change in the NADP$^+$/NADPH ratio (Fig. 2G) but a lower ratio of reduced GSH to oxidized glutathione (GSSG) (Fig. 2H). These results suggest that ALDH7A1 substantially affects redox homeostasis in the brain.

Because ALDH7A1 is directly involved in degradation of reactive aldehydes and NAD$^+$-dependent reactions, we hypothesized that brain redox homeostasis could be disrupted in ALDH7A1 KO$^{Global}$ mice due to redox dysfunction in astrocytes. To selectively examine redox changes in astrocytes, we engineered an adeno-associated virus (AAV) to selectively express a ratiometric redox sensor (mito-Grx1-roGFP2) (*47*) in astrocytes and injected it into the prelimbic cortex of cKO$^{Astro}$ mice (Fig. 2I). Compared to Con$^{Astro}$ mice, cKO$^{Astro}$ mice had a lower 488/405-nm ratio, indicative of a reduced GSH/GSSG ratio in astrocytes (Fig. 2, J and K). This result matches the reduced GSH/GSSG ratio observed in tissue homogenate from KO$^{Global}$ mice and suggests that ALDH7A1 depletion in astrocytes disrupts astrocyte redox homeostasis.

We then investigated the cell autonomous consequences of impaired redox homeostasis on redox-related functions in astrocytes. First, we looked for evidence of oxidative stress or mitochondrial dysfunction in astrocytes. Using CellROX, a cell-permeable dye that fluoresces upon oxidation, we did not detect significant increases in reactive oxygen species (ROS) in astrocytes by flow cytometry (fig. S3, A to C). We also performed Seahorse analysis of cellular respiration in primary astrocytes and found no changes in cellular respiration at baseline or under mitochondrial stress (fig. S3D). Together, these results suggested that global ALDH7A1 depletion did not elicit robust oxidative stress in astrocytes at the levels frequently associated with cell and tissue damage.

Next, we assessed the cell autonomous effects of ALDH7A1 depletion on astrocyte redox homeostasis in vivo. For these experiments, we used a "mosaic deletion" strategy (*48*) to generate mice with *Aldh7a1*-deleted and *Aldh7a1*-undeleted astrocytes intermixed within the same animal {*Aldh7a1*$^{flox/flox}$; BAC-*Slc1a3*$^{CreER}$; *R26-LSL-mGCaMP3*$^{flox/+}$ mice [cKO$^{Astro(Mosaic)}$]}. By using a less efficient strain of *Slc1a3*$^{CreER}$ [Tg(Slc1a3-cre/ERT)1Nat/J], we were able to delete *Aldh7a1* in ~50% of cortical astrocytes and sparsely label ALDH7A1-immunopositive (ALDH7A1$^+$) and ALDH7A1-immunonegative (ALDH7A1$^-$) astrocytes with membrane-bound GCaMP3, an effective readout of ROS-sensitive $Ca^{2+}$ signaling events in astrocyte processes (*49*) (Fig. 2L and fig. S3E). ALDH7A1$^+$ and ALDH7A1$^-$ astrocytes had a similar expression of an astrocyte reactivity marker, glial fibrillary acidic protein (GFAP), and an oxidative stress marker, 8-oxo-dG (fig. S3, F and G), which suggested that no gross changes in cellular reactivity or robust oxidative stress occur in astrocytes in vivo. We then assessed astrocyte intracellular $Ca^{2+}$ signaling in acute cortical brain slices from the prelimbic cortex (Fig. 2, M to O). At baseline, neither the frequency nor amplitude of $Ca^{2+}$ transients (Fig. 2, P and Q), nor the number of active microdomains (Fig. 2R), were different between ALDH7A1$^+$ and ALDH7A1$^-$ cells, suggesting that ALDH7A1$^-$ cells did not have altered $Ca^{2+}$ signaling under normative conditions. However, following brief, low-dose exposure to *tert*-butyl hydrogen peroxide (tBHP), a compound that stimulates ROS production (*50*), the frequency of $Ca^{2+}$ transients was significantly higher in ALDH7A1$^-$ cells than ALDH7A1$^+$ cells (Fig. 2P). These results indicated that ALDH7A1-deficient astrocytes had an increased sensitivity to redox imbalance. Together, these results implied a role of ALDH7A1 in astrocyte redox homeostasis at both molecular expression (Fig. 2, A to K, and table S1) and functional (Fig. 2, L to R) levels, unaccompanied by robust oxidative stress or cell damage (fig. S3, A to G).

### SFN ameliorates maladaptive affective behaviors, but not seizure susceptibility, in ALDH7A1 KO mice

To determine whether astrocyte redox imbalance is a major contributor to brain and behavioral phenotypes in ALDH7A1 KO mice, we tested the impact of treating mice with SFN, a brain-penetrant antioxidant derived from broccoli sprouts. SFN helps cells maintain redox homeostasis by inducing expression of cytoprotective, catalytic enzymes via the NRF2 pathway (*51*, *52*). To administer SFN, we developed a dietary formulation that remained stable and bioactive in rodent chow (fig. S4A). At baseline, cKO$^{Astro}$ mice had reduced NRF2 protein levels in astrocytes, but 1-week dietary administration of SFN was sufficient to normalize NRF2 levels (fig. S4, B to E), suggesting that dietary SFN can successfully increase antioxidant protection in ALDH7A1-deficient astrocytes.

We then investigated the impact of long-term dietary SFN administration on the behavior of cKO$^{Astro}$ and KO$^{Global}$ mice (Fig. 3, A and B). This long-term administration of SFN from 3 weeks of age

Downloaded from https://www.science.org on August 04, 2026

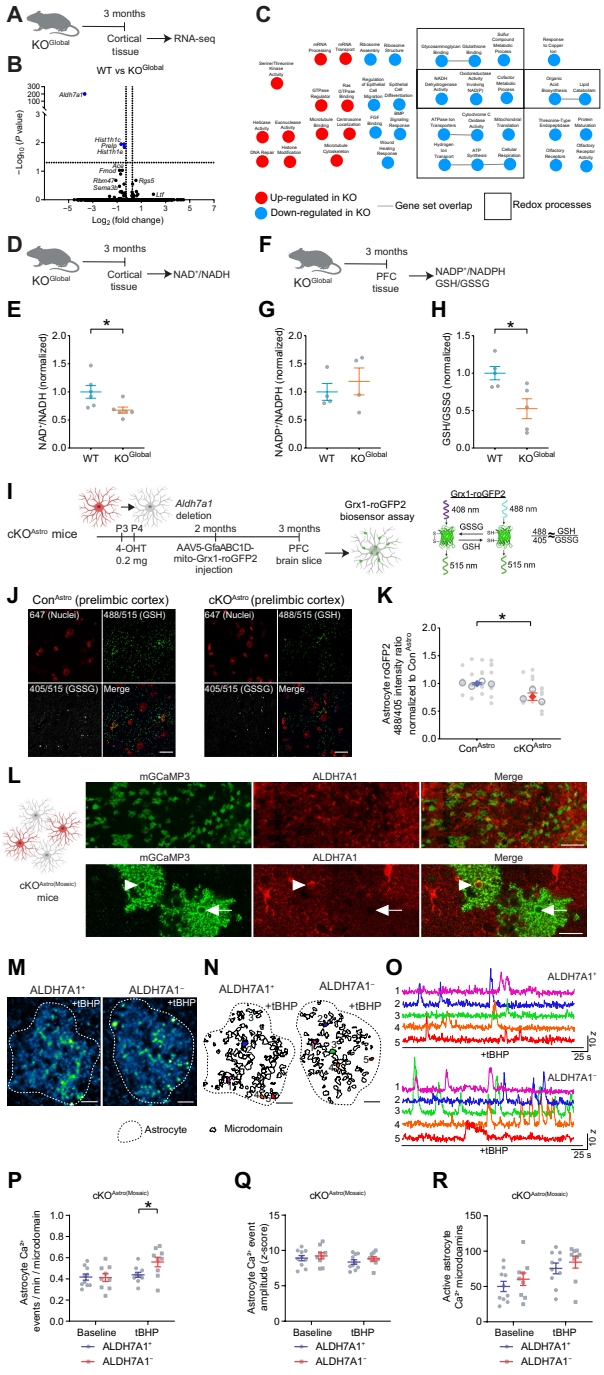


**Fig. 2. Astrocyte ALDH7A1 regulates cellular redox homeostasis.** (**A**) Experimental design for (B) and (C). (**B**) Volcano plot of the RNA-seq from KO$^{Global}$ and WT mice. Dotted lines indicate cutoffs at $P < 0.05$ and $\log_2$(fold change) > |1.2|. (**C**) EnrichmentMap summary of the GSEA of KO$^{Global}$ cortical tissue. Redox-related pathways are outlined. (**D**) Experimental design for (E). (**E**) $NAD^+$/NADH ratio in cortical homogenates from KO$^{Global}$ and WT mice ($n = 6$ mice; $^*P < 0.05$). (**F**) Experimental design for (G) and (H). (**G** and **H**) $NADP^+$/NADPH ratio (G) and GSH/GSSG ratio (H) in PFC homogenates from KO$^{Global}$ and WT mice ($NADP^+$/NAPDH: $n = 4$ mice; $P > 0.05$; GSH/GSSG: $n = 5$ mice; $^*P < 0.05$). (**I**) Schematic of the astrocyte-specific mito-Grx1-roGFP2 redox sensor assay. (**J**) Representative oxidized (405/515) and reduced (488/515) mito-Grx1-roGFP2 fluorescence with TO-PRO nuclear labeling in cKO$^{Astro}$ and Con$^{Astro}$ mice. Scale bars, 20 μm. (**K**) Quantification of the mito-Grx1-roGFP2 488/405 fluorescence ratio in cKO$^{Astro}$ and Con$^{Astro}$ mice [$n = 3$ to 4 mice (open circles), five to nine images per mouse (filled circles); $^*P < 0.05$]. (**L**) Left: Schematic of ALDH7A1 depletion in cKO$^{Astro(Mosaic)}$ mice. Right: Representative ALDH7A1 and mGCaMP3 immunofluorescence. Scale bars, 200 μm (top) and 20 μm (bottom). Arrowhead: ALDH7A1$^+$; arrow: ALDH7A1$^-$ astrocyte. (**M**) Median projections (540 frames, pseudocolored) of one ALDH7A1$^+$ astrocyte (outlined; left) and one ALDH7A1$^-$ astrocyte (right) after tBHP. Scale bars, 10 μm. (**N**) Microdomain maps from one ALDH7A1$^+$ astrocyte (left) and one ALDH7A1$^-$ (right) after tBHP. Cell borders outlined. Scale bars, 10 μm. (**O**) $Ca^{2+}$ traces from five microdomains in ALDH7A1$^+$ and ALDH7A1$^-$ astrocytes after tBHP. (**P** to **R**) Microdomain $Ca^{2+}$ transient frequency (P), amplitude (Q), and number of active microdomains (R) at baseline and after tBHP ($n = 9$ to 10 cells; $^*P < 0.05$). Data in [(E) to (H), (K), and (P) to (R)] represent means ± SEM. Statistics: Student's *t* test [(E), (G), and (H)]; nested *t* test (K); repeated-measures two-way ANOVA with Holm-Sidak post hoc test [(P) to (R)]. Graphic elements created in BioRender. Faust, T. (2026) https://BioRender.com/wu62fdy.

Downloaded from https://www.science.org on August 04, 2026

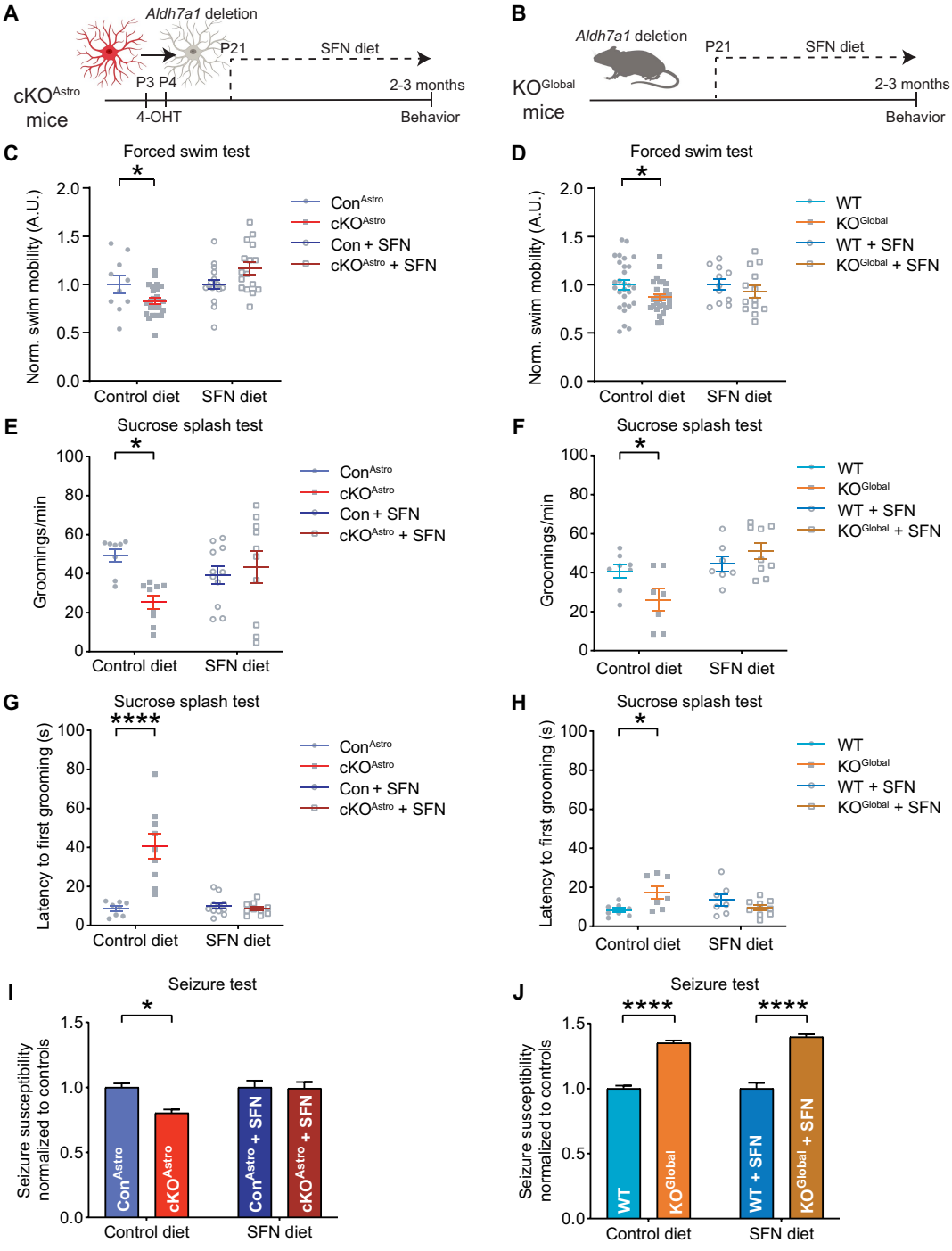


**Fig. 3. SFN ameliorates maladaptive affective behaviors, but not seizure susceptibility, in ALDH7A1 KO mice.** (**A** and **B**) Schematic of the behavioral assessment in cKO$^{Astro}$ mice (A) and KO$^{Global}$ mice (B) after long-term dietary SFN treatment. (**C** and **D**) FST: time swimming in cKO$^{Astro}$ versus Con$^{Astro}$ mice (C) and KO$^{Global}$ versus WT mice (D) on control diet or SFN diet ($n$ = 10 to 28 mice). Data are from Fig. 1 (G and M) and fig. S5 (C and D), normalized to matched dietary controls; significance reflects the original within-experiment statistical comparisons (*$P$ < 0.05). A.U., arbitrary units. (**E** to **H**) Sucrose splash test: grooming frequency and latency to grooming in cKO$^{Astro}$ versus Con$^{Astro}$ (E and G) and KO$^{Global}$ versus WT mice (F and H) on control or SFN diet ($n$ = 7 to 11 mice; *$P$ < 0.05, ****$P$ < 0.0001). Control diet data are from Fig. 1 (H and N). (**I** and **J**) PTZ seizure susceptibility in cKO$^{Astro}$ versus Con$^{Astro}$ (I) and KO$^{Global}$ versus WT mice (J) on control diet or SFN diet. Data show normalized $EC_{50}^{-1}$ values from PTZ dose-response curves (cKO$^{Astro}$: $n$ = 5 to 8 mice, KO$^{Global}$: $n$ = 8 to 12 mice; *$P$ < 0.05, ****$P$ < 0.0001). Data are from Fig. 1 (F and L) and fig. S5 (E and F). All data represent means ± SEM. Statistics: Student's $t$ tests for original comparisons in Fig. 1 (G and M) and fig. S5 (C and D); two-way ANOVA with Holm-Sidak post hoc test [(E) to (J)]. Graphic elements created in BioRender. Faust, T. (2026) https://BioRender.com/gu9169z.

Downloaded from https://www.science.org on August 04, 2026

until adulthood was well tolerated and did not affect animal body weight (fig. S5, A and B). In both cKO$^{Astro}$ and KO$^{Global}$ mice, SFN treatment normalized the maladaptive affective behaviors. When treated with SFN, neither cKO$^{Astro}$ mice nor KO$^{Global}$ mice exhibited abnormal FST behavior (Fig. 3, C and D, and fig. S5, C and D) or abnormal sucrose splash test behavior (Fig. 3, E to H). In contrast, SFN differentially influenced seizure threshold in cKO$^{Astro}$ and KO$^{Global}$ mice. The lower seizure susceptibility observed in cKO$^{Astro}$ mice was normalized by SFN (Fig. 3I and fig. S5E), but KO$^{Global}$ mice still exhibited increased seizure susceptibility in the presence of SFN (Fig. 3J and fig. S5F), indicating that SFN was ineffective for treating the seizure-associated phenotype in KO$^{Global}$ mice. Together, these data suggest that SFN rescued the astrocyte-driven mechanisms of ALDH7A1 dysfunction, resulting in amelioration of astrocyte-driven maladaptive affective behaviors but not liver-driven mechanisms that increase seizure susceptibility.

### SFN ameliorates astrocyte ALDH7A1-induced neuronal hypoactivity in the prelimbic cortex

Because SFN was effective in rescuing maladaptive affective behaviors in both KO$^{Global}$ and cKO$^{Astro}$ mice, we next looked for the neural circuit that might connect astrocyte redox dyshomeostasis with maladaptive affective behaviors. Although multiple brain regions are involved in maladaptive affective behaviors, we prioritized the prelimbic cortex, a region known to regulate FST behavior (*42*) where we had observed both strong depletions in ALDH7A1 (Fig. 1J) and deficiencies in redox homeostasis (Fig. 2, F to R). Pharmacological lesioning experiments using ibotenic acid further suggested that the prelimbic cortex is also required for maladaptive affective behavior during the sucrose splash test (fig. S6). We therefore hypothesized that the prelimbic cortex may contribute to the maladaptive affective behaviors in KO$^{Global}$ and cKO$^{Astro}$ mice.

The specific neurons in the prelimbic cortex that control FST swimming activity are the L5 pyramidal neurons that project to the brainstem (*42*), with reductions in neuronal activity causing reduced swim mobility. To examine the activity of L5 pyramidal neurons in cKO$^{Astro}$ and KO$^{Global}$, we used AAV9-CaMKIIa-GCaMP6f to drive L5 pyramidal neuron expression of the fluorescent $Ca^{2+}$ indicator GCaMP6f (Fig. 4, A and B). Notably, when expressed here in neurons, instead of in astrocytes, spikes in GCaMP fluorescence serve as indicators of neuronal activity. Therefore, to assess neuronal activity, we prepared acute brain sections from the prelimbic cortex and imaged spontaneous changes in GCaMP6f fluorescence in the soma of L5 pyramidal neurons. In both cKO$^{Astro}$ mice (Fig. 4, C and D) and KO$^{Global}$ mice (fig. S7), there was a reduced frequency of somatic $Ca^{2+}$ events in prelimbic L5 pyramidal neurons, suggesting that these neurons were hypoactive. We then measured $Ca^{2+}$ event frequency in prelimbic L5 pyramidal neurons in brain slices from SFN-fed cKO$^{Astro}$ mice. Similar to the effect of SFN diet on maladaptive affective behaviors in vivo, the $Ca^{2+}$ event frequency of the prelimbic L5 pyramidal neurons in cKO$^{Astro}$ brain slices was normalized by SFN diet (Fig. 4, C and D). Thus, across cKO$^{Astro}$, KO$^{Global}$, and SFN-treated cKO$^{Astro}$ mice, the activity of L5 prelimbic pyramidal neurons correlated with maladaptive affective behaviors, suggesting that hypoactivity of L5 prelimbic pyramidal neurons underlies maladaptive affective behaviors in mice with ALDH7A1 depletion.

The prelimbic L5 pyramidal neuron hypoactivity is consistent with the maladaptive affective behaviors, but it is somewhat counterintuitive that neurons would be hypoactive in KO$^{Global}$ mice that are more susceptible to seizures. To further confirm the reduced activity of prelimbic L5 pyramidal neurons and interrogate the contribution of these neurons to PTZ-induced seizures, we performed immunostaining for c-FOS, a marker of neuronal activity, in tissue from KO$^{Global}$ and WT mice collected at 1 hour after PTZ-induced seizures. For consistency, we only included mice with a seizure severity score of 7 on the modified Racine scale. Compared to the dentate gyrus where ~90% of cells were c-FOS$^+$ in both WT and KO$^{Global}$ mice, only ~1 to 3% of cells were c-FOS$^+$ in L5 of the prelimbic cortex, suggesting that the prelimbic cortex is not a major driver of seizure activity (fig. S8). In addition, the number of c-FOS$^+$ cells in the L5 prelimbic cortex was significantly lower in KO$^{Global}$ mice than in WT mice (fig. S8, F and G), further confirming our findings that neuronal activity is reduced in the prelimbic cortex.

Having identified prelimbic L5 pyramidal neurons as an SFN-responsive neural correlate of maladaptive affective behaviors in ALDH7A1 KO mice, we sought to determine whether the change in prelimbic L5 pyramidal neuron activity is due to synaptic changes or the electrical properties of the neurons. To assess synaptic inputs on prelimbic L5 pyramidal neurons, we recorded excitatory postsynaptic currents (ESPCs) and inhibitory postsynaptic currents (IPSCs) from prelimbic L5 pyramidal neurons. We observed no difference in the frequency or amplitude of spontaneous EPSCs (sEPSCs) and spontaneous IPSCs (sIPSCs) in cKO$^{Astro}$ mice (fig. S9, A to D) and KO$^{Global}$ mice (fig. S9, E to H), suggesting that prelimbic L5 pyramidal neuron hypoactivity is not due to changes in synaptic inputs. We next measured the intrinsic electrical properties of prelimbic L5 pyramidal neurons in KO$^{Global}$ mice. Action potential shape was unaffected, as were capacitance, and membrane resistance (fig. S10, A to C). However, the resting membrane voltage of the neurons was more hyperpolarized (fig. S10D), which can lead to fewer spikes given a fixed amount of synaptic input. Consistent with this result, depolarizing current injections elicited fewer action potentials across a range of current amplitudes (fig. S10E), suggesting that the prelimbic L5 pyramidal neuron hypoactivity in ALDH7A1 KO mice was due to a reduction in neuronal excitability.

Next, we investigated how dietary SFN restores neuronal activity in ALDH7A1-deficient mice. Immunolabeling revealing increased NRF2 in astrocytes after dietary SFN (fig. S4, C to D), suggesting that SFN acts by restoring redox imbalance in astrocytes. To test whether restoring astrocyte function alone is sufficient to normalize neuronal activity, we generated an astrocyte-specific ALDH7A1 Rescue AAV (AAV5-GfaABC1D-ALDH7A1-mCherry) and injected it into the prelimbic cortex of adult cKO$^{Astro}$ mice (Fig. 4E and fig. S11A). The virus was expressed selectively in astrocytes (fig. S11B) and restored ALDH7A1 protein levels (fig. S11C). In cKO$^{Astro}$ mice injected with control AAV, neuronal $Ca^{2+}$ event frequency was reduced compared to Con$^{Astro}$ mice, whereas ALDH7A1 Rescue AAV restored $Ca^{2+}$ event frequency to control levels (Fig. 4, E and F). Thus, neuronal hypoactivity can be reversed by correcting astrocyte ALDH7A1 deficiency, demonstrating that astrocyte-dependent regulation of neuronal activity remains reversible in adulthood.

To further test whether SFN restores neuronal activity by normalizing astrocyte redox signaling via NRF2 signaling, we used a complementary genetic strategy. NRF2 protein stability and its function as a master transcription factor (TF) are regulated by KEAP1, which targets NRF2 for ubiquitination and degradation (*53*). SFN inhibits

Downloaded from https://www.science.org on August 04, 2026

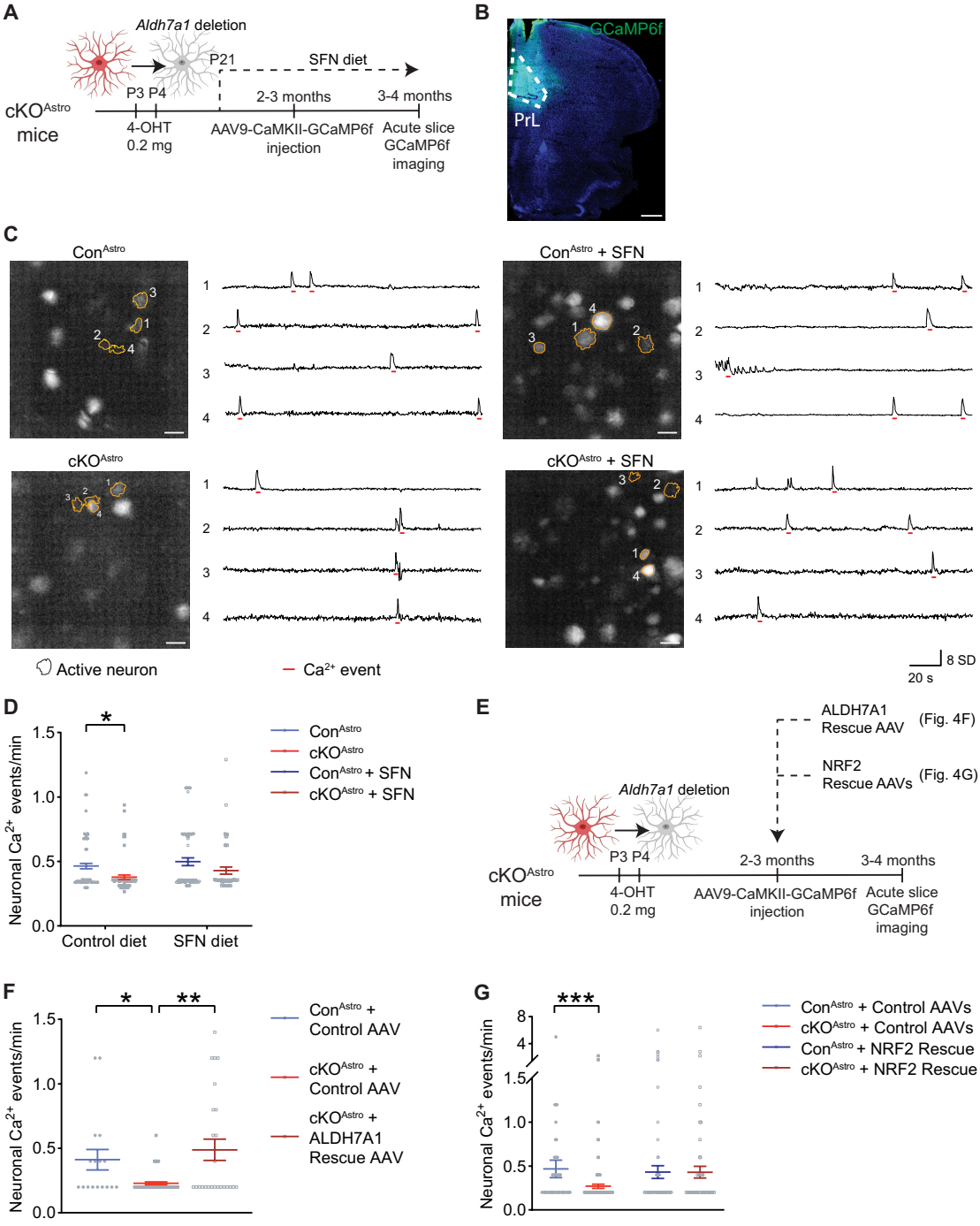


**Fig. 4. SFN ameliorates astrocyte ALDH7A1-induced neuronal hypoactivity in the prelimbic cortex.** (**A**) Experimental design for assessing the prelimbic L5 pyramidal neuron activity in cKO$^{Astro}$ mice by GCaMP6f fluorescence after long-term dietary SFN treatment. (**B**) Representative GCaMP6f fluorescence in cKO$^{Astro}$ mice after stereotactic injection of AAV9-CaMKII-GCaMP6f into the prelimbic cortex (PrL). Scale bar, 500 μm (**C**) Representative images (left) and traces (right) of GCaMP6f fluorescence in prelimbic L5 pyramidal neurons from cKO$^{Astro}$ and Con$^{Astro}$ mice on control or SFN diet. Numbered outlines indicate neurons shown in traces and included in analysis. Events are indicated by red underlines. Scale bars, 20 μm. (**D**) Prelimbic L5 pyramidal neuron $Ca^{2+}$ event frequency in cKO$^{Astro}$ and Con$^{Astro}$ mice on control diet or SFN diet ($n = 49$ to 101 neurons; $^{*}P < 0.05$). (**E**) Experimental design for (F) to (G). (**F**) Prelimbic L5 pyramidal neuron $Ca^{2+}$ event frequency in Con$^{Astro}$ and cKO$^{Astro}$ mice after injection of ALDH7A1 Rescue AAV (AAV5-GfaABC1D-ALDH7A1-mCherry) or control AAV(AAV5-GfaABC1D-mCherry) ($n = 17$ to 62 neurons; $^{*}P < 0.05$, $^{**}P < 0.01$). (**G**) Prelimbic L5 pyramidal neuron $Ca^{2+}$ event frequency in Con$^{Astro}$ and cKO$^{Astro}$ mice after injection of NRF2 Rescue AAVs (AAV5-GfaABC1D-Nrf2-mCherry and AAV5-GfaABC1D-*Keap1* shRNA) or control AAVs (AAV5-GfaABC1D-mCherry and AAV5-GfaABC1D-scrambled shRNA) ($n = 50$ to 115 neurons; $^{***}P < 0.001$). All data represent means ± SEM. Statistics: Mann-Whitney with Holm-Sidak multiple comparisons test [(D) and (G)]; Kruskal-Wallis test with Dunn's post hoc test (F). Graphic elements created in BioRender. Faust, T. (2026) https://BioRender.com/o3kqr4h.

Downloaded from https://www.science.org on August 04, 2026

KEAP1, thereby preventing NRF2 degradation and sustaining NRF2 signaling (*54*). To mimic the effects of SFN on NRF2 signaling, we generated two astrocyte-specific NRF2 Rescue AAVs: one to overexpress *Nrf2* (GfaABC1D-Nrf2-mCherry) and one to knock down *Keap1* [GfaABC1D-mCherry-*Keap1* short hairpin RNA (shRNA)] (fig. S11A). Coexpression of both constructs increased NRF2 levels in astrocytes (fig. S11D), confirming the validity of this approach. Similarly to the ALDH7A1 Rescue AAV, injection of NRF2 Rescue AAVs into the prelimbic cortex of $cKO^{Astro}$ restored neuronal $Ca^{2+}$ event frequency to control levels (Fig. 4, E and G). Together, these findings show that prelimbic neuronal hypoactivity results from astrocyte redox dysregulation caused by ALDH7A1 deficiency and can be reversibly corrected by restoring ALDH7A1 or activating the NRF2 pathway in astrocytes, including through dietary SFN.

### SFN ameliorates expression of ion channel and ion transporter gene pathways in $cKO^{Astro}$ astrocytes

How does redox imbalance in astrocytes lead to changes in neuronal resting voltage and neuronal activity? One possibility is that redox imbalance in astrocytes could impair astrocyte regulation of ion concentrations in the extracellular space, both through the activity of ion channels and transporters and by changing the volume of the extracellular space (*55*). Such changes in extracellular ion concentrations would directly alter neuronal resting membrane voltage. Astrocytes could also release trophic factors and signaling molecules that can influence the expression of neuronal ion channels and transporters (*56*). To determine how redox imbalance in astrocytes drives changes in neuronal activity, we performed RNA-seq on cortical astrocytes isolated from four groups of animals: $Con^{Astro}$, $cKO^{Astro}$, SFN-fed $Con^{Astro}$, and SFN-fed $cKO^{Astro}$ (Fig. 5A and fig. S12A). *Aldh7a1* and *Slc1a3* were significantly different between astrocytes isolated from $cKO^{Astro}$ versus $Con^{Astro}$ mice as well as SFN-fed $cKO^{Astro}$ versus SFN-fed $Con^{Astro}$ (fig. S12B and table S1), reasonably reflecting the animals' genotype (*Aldh7a1*$^{Flox/Flox}$; *Slc1a3*$^{CreER/+}$). However, similar to the RNA-seq data from $KO^{Global}$ brain tissue (Fig. 2B), only six other genes were significantly different between $cKO^{Astro}$ and $Con^{Astro}$ mice (*Acer2*, *Vsig2*, *Esr1*, *Foxd1*, *Echdc3*, and *A630020A06*; fig. S12B and table S1). We therefore performed pathway analysis by GSEA to identify significant gene sets (pathways) potentially implicated in the SFN rescue of neuronal hypoactivity caused by astrocyte ALDH7A1 deficiency (Fig. 5B and table S1). We focused on pathways with the following characteristics: (i) differentially expressed between untreated $cKO^{Astro}$ and untreated $Con^{Astro}$ astrocytes, (ii) rescued in SFN-fed $cKO^{Astro}$ astrocytes (i.e., no difference between SFN-fed $cKO^{Astro}$ and untreated $Con^{Astro}$ astrocytes), and (iii) dissimilarly affected by SFN in $Con^{Astro}$ versus $cKO^{Astro}$ astrocytes. Among the 262 pathways that fit these criteria (Fig. 5C), we identified 12 pathways related to ion channels and ion transporters as strong candidate pathways that could contribute to reduced neuronal resting voltage (Fig. 5D). On the basis of this bioinformatic analysis, we developed a working hypothesis that changes in astrocyte ion transporters and ion channels alter local extracellular ion concentrations, thereby contributing to prelimbic L5 neuronal hypoactivity in $cKO^{Astro}$ mice.

Astrocytes regulate extracellular potassium concentration $[K^+]$ through multiple mechanisms, including active transport via $Na^+$- and $K^+$-dependent ATPases ($Na^+,K^+$-ATPases) (*57*) and passive conductance mediated by two-pore $K^+$ channels (*58*) and inward-rectifying $K^+$ channels, including $K_{ir4.1}$ (*55*). Within the "core enrichment" of the 12 ion channel and ion transporter pathways (i.e., the subset of genes that contribute most strongly to pathway significance; table S1), we identified genes encoding several subunits of $Na^+,K^+$-ATPases (*Atp1a1*, *Atp1a2*, *Atp1a3*, *Atp1b1*, *Atp1b2*, and *Atp1b3*) and two-pore $K^+$ channels (*Kcnk1*, *Kcnk2*, *Kcnk3*, *Kcnk4*, *Kcnk5*, *Kcnk7*, *Kcnk12*, and *Kcnk13*), whereas *Kcnj10* ($K_{ir4.1}$) was not represented within the core enrichment. Thus, although no individual subunit met our threshold for differential expression, pathway analysis suggested that astrocytic ion-homeostasis mechanisms involving $Na^+,K^+$-ATPases and two-pore $K^+$ channels could be altered. Because $Na^+,K^+$-ATPases are major astrocytic regulators of extracellular $K^+$ homeostasis and neuronal resting membrane voltage, and because multiple $Na^+,K^+$-ATPase subunits were represented within the GSEA core enrichment, we prioritized $Na^+,K^+$-ATPases for functional follow-up. Two-pore $K^+$ channels were also considered but were not pursued further due to limited specificity of available pharmacological tools.

To test whether astrocytic changes in $Na^+,K^+$-ATPases underlie the prelimbic L5 neuron hypoactivity, we applied a pharmacological inhibitor of $Na^+,K^+$-ATPases (50 μM ouabain) to acute brain slices and measured the effect on the prelimbic L5 pyramidal neuron $Ca^{2+}$ event frequency (Fig. 5, E and F). Our hypothesis was that blocking $Na^+,K^+$-ATPases would rescue the neuronal hypoactivity. Consistent with prior experiments (Fig. 4), prelimbic L5 pyramidal neuron $Ca^{2+}$ event frequency was significantly lower in $cKO^{Astro}$ mice compared with that in $Con^{Astro}$ mice. Within 3 to 6 min after the application of ouabain, $Ca^{2+}$ event frequency in $cKO^{Astro}$ neurons significantly increased, reaching the levels in $Con^{Astro}$ mice, whereas $Ca^{2+}$ event frequency in $Con^{Astro}$ mice neurons did not significantly increase in this time frame, suggesting that excess astrocytic $Na^+,K^+$-ATPase activity, and associated reductions in extracellular $[K^+]$, are responsible for the prelimbic L5 pyramidal neuron hypoactivity. These data provide physiological validation of the bioinformatic inferences from $cKO^{Astro}$ astrocyte gene expression data.

Last, we sought to determine whether the identified changes of ion transporter and ion channel genes in $cKO^{Astro}$ astrocyte were under the influence of astrocyte redox status and SFN. To address this multifactorial question, we used the Causal Inference Engine (CIE) analysis platform (*59*), a bioinformatic approach to infer the activity of transcriptional regulators by comparing gene expression patterns of ion channel and ion transporter genes in $cKO^{Astro}$ astrocytes to the chromatin immunoprecipitation sequencing (ChIP-seq) atlas, a publicly available database of TF-gene regulatory networks (fig. S12C). We restricted our analysis to the 432 ion channel and ion transporter genes that were identified by GSEA as the most significantly changed in the in $cKO^{Astro}$ astrocytes (the "core enrichment" of the 12 ion channel and ion transporter pathways; table S1). We identified TFs with significant differences in predicted activation in untreated $cKO^{Astro}$ versus untreated $Con^{Astro}$ astrocytes but not in SFN-fed $cKO^{Astro}$ or SFN-fed $Con^{Astro}$ astrocytes versus untreated $Con^{Astro}$ astrocytes (fig. S12D). This list included ZBTB17, ZEB1, BRD2, SMAD1, FOXF2, GREB1, TET2, and GATA4, several of which are known to be redox-sensitive transcriptional regulators (*60*–*63*). Together, these bioinformatic analyses indicated that astrocyte ion channel and ion transporter gene changes in $cKO^{Astro}$ mice are, at least in part, downstream of altered astrocyte redox homeostasis. Accordingly, an SFN-driven restoration of redox homeostasis was likely to provide the rescue effect.

Downloaded from https://www.science.org on August 04, 2026

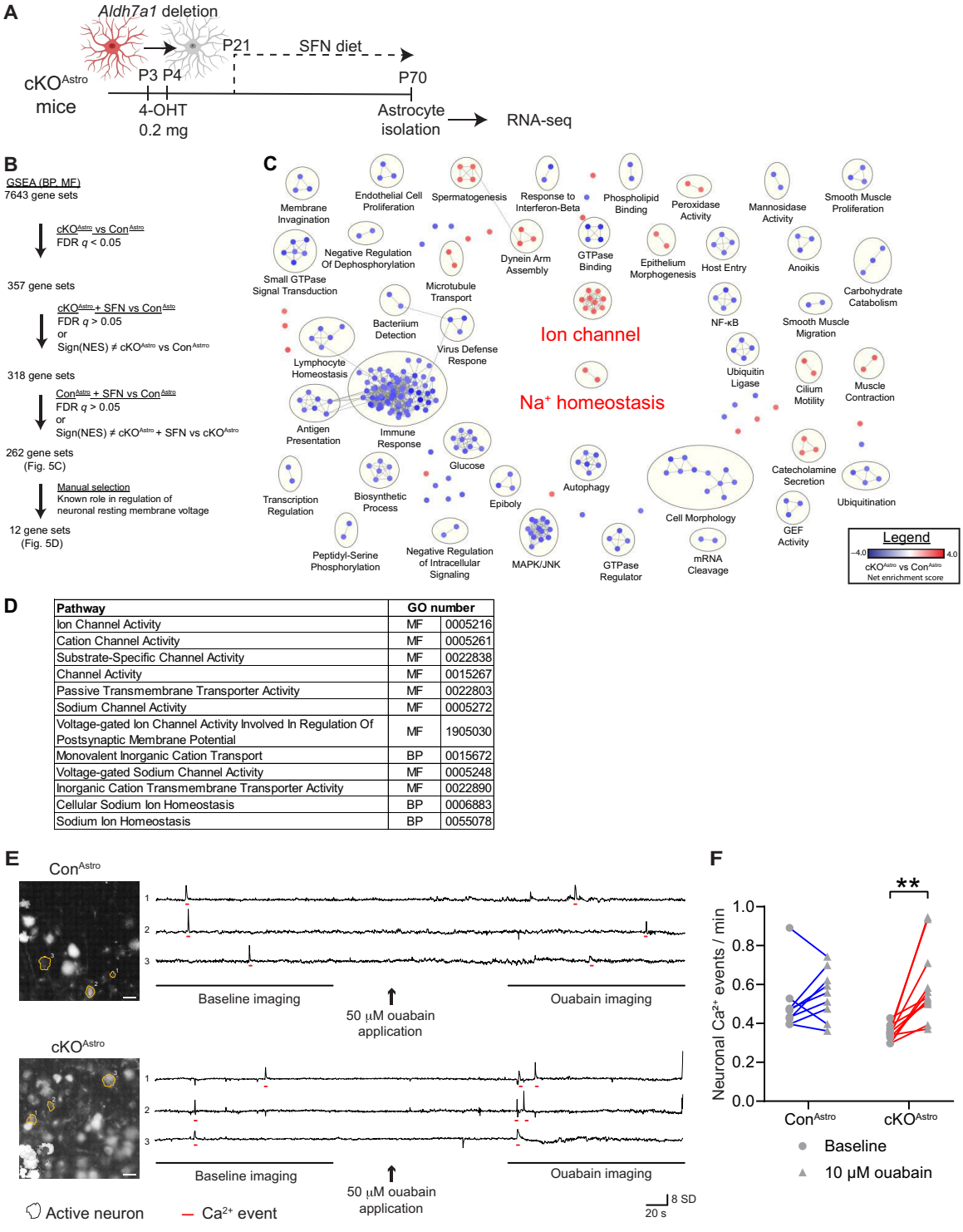


**D**

| Pathway | GO number | |
|---|---|---|
| Ion Channel Activity | MF | 0005216 |
| Cation Channel Activity | MF | 0005261 |
| Substrate-Specific Channel Activity | MF | 0022838 |
| Channel Activity | MF | 0015267 |
| Passive Transmembrane Transporter Activity | MF | 0022803 |
| Sodium Channel Activity | MF | 0005272 |
| Voltage-gated Ion Channel Activity Involved In Regulation Of Postsynaptic Membrane Potential | MF | 1905030 |
| Monovalent Inorganic Cation Transport | BP | 0015672 |
| Voltage-gated Sodium Channel Activity | MF | 0005248 |
| Inorganic Cation Transmembrane Transporter Activity | MF | 0022890 |
| Cellular Sodium Ion Homeostasis | BP | 0006883 |
| Sodium Ion Homeostasis | BP | 0055078 |




**Fig. 5. SFN ameliorates expression of ion channel and ion transporter gene pathways in cKO$^{Astro}$ astrocytes.** (**A**) Experimental design for the RNA-seq of cortical astrocytes isolated from cKO$^{Astro}$, cKO$^{Astro}$ + SFN, Con$^{Astro}$, and Con$^{Astro}$ + SFN mice. (**B**) Post hoc filtering workflow for GSEA, narrowing 7643 affected gene sets to 262 showing genotype-specific rescue by SFN. (**C**) Network visualization of the 262 gene sets identified in (B). Circles represent gene sets color by normalized enrichment score (cKO$^{Astro}$ versus Con$^{Astro}$). Gray lines indicate overlapping genes. Yellow outlines indicate major biological themes. (**D**) Table of the 12 ion channels and $Na^+$ homeostasis gene sets highlighted in (C). (**E**) Representative images (left) and traces (right) of GCaMP6f fluorescence in Con$^{Astro}$ and cKO$^{Astro}$ mice. Numbered outlines indicate neurons shown in traces. Events are indicated by red underlines. Analysis windows are underlined in black. Arrows indicate 50 μM ouabain application. Scale bars, 20 μm. (**F**) Prelimbic L5 pyramidal neuron $Ca^{2+}$ event frequency in Con$^{Astro}$ and cKO$^{Astro}$ mice at baseline and after 50 μM ouabain application ($n = 9$ brain sections; $^{**}P < 0.01$). Data in (F) represent individual brain slices, at baseline and after ouabain application. Statistics: two-way repeated measures ANOVA with Holm-Sidak post hoc test (F). Graphic elements created in BioRender. Faust, T. (2026) https://BioRender.com/rsylogn.

Downloaded from https://www.science.org on August 04, 2026

## DISCUSSION

The present study includes three major findings with implications for both basic and translational neuroscience. First, using animal models for a monogenic epilepsy, PDE, we dissociate two distinct brain pathophysiologies caused by liver-astrocyte pleiotropy: Seizures are caused by hepatic ALDH7A1 depletion whereas maladaptive affective behaviors are caused by astrocytic ALDH7A1 depletion. Second, using cell type–specific manipulations, we define an astrocyte-initiated mechanism underlying maladaptive affective behaviors: ALDH7A1-dependent redox dysfunction in astrocytes causes prelimbic L5 pyramidal neuron hypoactivity linked to $Na^+$,$K^+$-ATPase–dependent reductions in extracellular [$K^+$] that reduce neuronal resting membrane voltage. Last, we demonstrate that this mechanism in astrocytes is therapeutically actionable: NRF2 activation in astrocytes by viral and dietary approaches restores prelimbic activity and normalizes maladaptive affective behaviors, providing an opportunity for pathway-specific, cell type–targeted therapies orthogonal to antiseizure therapy.

Monogenic diseases can provide insight into the etiology of complex brain disorders, but many display pleiotropy across tissues and cell types, motivating cell type–specific mechanistic investigations. This strategy has been informative for neurodevelopmental disorders such as tuberous sclerosis (*TSC1/2* mutations), Rett's syndrome (*MECP2* mutations), and Fragile-X syndrome (*FMR1* mutations) where both astrocytes and neurons shape distinct aspects of disease pathology (*64*–*66*). Our findings suggest that it is also important to consider gene function outside the central nervous system (CNS), including how peripheral pathologies may affect the brain. Glial cells share several functional specializations with peripheral cell types, raising the possibility that certain symptom clusters under monogenic conditions reflect contributions from both CNS and peripheral perturbations. For example, both astrocytes and hepatocytes have specialized roles in performing metabolic and detoxification functions for the brain and for the body, resulting in a large overlap between astrocyte-enriched and hepatocyte-enriched genes (e.g., *ALDH1L1*, *APOE*, *SOD1*, *GLUL*, *FABP7*, *CLU*, *GCLM*, and *C3*) (*67*, *68*). In the case of *ALDH7A1* mutations, this shared biology is reflected in a combination of hepatic abnormalities that reduce seizure threshold, reminiscent of established mechanisms of hepatic-induced seizures (*69*–*72*), and astrocyte-dependent changes in prelimbic neuronal activity and maladaptive affective behaviors. Notably, ALDH7A1 ablation in the liver and in astrocytes may influence different brain regions in different ways, which has parallels to patterns of focal hypo- and hyperactivity reported in epilepsy (*73*–*76*). Because *Slc1a3*$^{CreER}$ does not achieve complete recombination in all astrocytes across the brain, we cannot fully exclude the possibility that incomplete recombination limited detection of a seizure-susceptibility phenotype in cKO$^{Astro}$ mice. However, we consider this unlikely to fully explain the absence of a seizure phenotype because *Emx1*$^{Cre}$-mediated deletion in astrocytes, oligodendrocytes, and excitatory neurons throughout cortex and hippocampus likewise did not increase seizure susceptibility, whereas liver-specific deletion was sufficient to do so. Together, these findings support hepatic ALDH7A1 loss as the dominant driver of seizure susceptibility in KO$^{Global}$ mice.

The mechanism linking astrocyte ALDH7A1 dysfunction with maladaptive affective behaviors aligns with emerging evidence that astrocytic regulation of neuronal activity plays a central role in mood disorders, particularly through $K^+$ homeostasis. Extracellular [$K^+$] affects neuronal activity by setting the neuronal membrane potential and is controlled by astrocytes via Kir4.1 and $Na^+$,$K^+$-ATPases (*77*, *78*). Both pathways have been implicated in depression (*79*, *80*). Kir4.1 protein levels are up-regulated in the postmortem parietal cortex from patients with MDD (*81*) and astrocyte-specific manipulation of Kir4.1 in the lateral habenula alters ketamine-responsive maladaptive affective behaviors in rodent models (*82*). Likewise, $Na^+$,$K^+$-ATPase subunit genes have decreased expression in patients with MDD and bipolar disorder (BD) (*83*, *84*) and are genetically linked to BD (*84*). *Atp1a3* haploinsufficiency in mice also increases vulnerability to stress-induced depression-like phenotypes (*85*). These findings converge with our data showing that astrocyte $Na^+$,$K^+$-ATPases in the prelimbic cortex can modulate maladaptive affective behaviors by reducing extracellular [$K^+$] and neuronal activity. However, a limitation of our pharmacological approach is that ouabain, although preferentially inhibiting astrocytic ATPases at the concentration used, may also weakly affect neuronal ATPases (*86*). More broadly, astrocyte morphology, gap-junction coupling, and $Ca^{2+}$ signaling are all altered by stress and antidepressant treatment (*87*–*89*), suggesting that redox-dependent and activity-dependent astrocyte-neuron interactions could represent a common pathophysiological pathway in mood disorders, distinct from seizure pathophysiology.

Future work is needed to more fully understand how ALDH7A1 deficiency in the liver elicits seizure pathology in the brain. Current models suggest that ALDH7A1 dysfunction leads to build up of metabolic intermediates that inactivate vitamin B6 (i.e., pyridoxine), which then inhibits over 100 enzymatic reactions in the brain that require vitamin B6 cofactor activity (*8*). The respective contributions of liver ALDH7A1 and astrocyte ALDH7A1 to vitamin B6 activity in the brain remain unknown. KO$^{Global}$ mice do not exhibit visually detectable spontaneous seizures, which is ideal for distinguishing the direct effects of ALDH7A1 from secondary pathologies resulting from seizures but phenotypically different from humans with PDE who suffer spontaneous seizures. Work from other murine models of ALDH7A1 ablation suggest that this apparent interspecies difference is largely due to diet rather than lack of homology—ALDH7A1 KO mice do not have spontaneous seizures on a standard lab mouse diet but exhibit spontaneous seizures when dietary lysine is increased or dietary pyridoxine is decreased (*30*, *90*). Likewise, dietary changes in lysine and pyridoxine consumption can prevent spontaneous seizures in humans with PDE (*91*). In the current study, we use PTZ-induced seizures as a readout of seizure risk, which is reduced in KO$^{Global}$ mice and responsive to pyridoxine supplementation, suggesting that it is an effective readout of the brain metabolic state underlying seizures in humans that can be shifted up or down through dietary modifications of lysine and pyridoxine but relatively insensitive to astrocyte ALDH7A1 ablation.

Our work provides preclinical evidence that an indirect antioxidant approach such as dietary SFN may be an effective supplemental therapy for treating psychiatric symptoms in patients with PDE in combination with antiseizure therapies. Current clinical approaches, designed to combat metabolic deficiencies in vitamin B6 elicited by impairments in the lysine degradation pathway, rely on pyridoxine supplementation, which is effective in controlling seizures but cannot treat mental/cognitive functions in patients with PDE (*46*). Our data suggest that the selective effectiveness of pyridoxine is because pyridoxine treats the hepatic ALDH7A1 pathophysiology underlying seizures but is ineffective in treating astrocyte ALDH7A1 pathophysiology underlying other aspects of PDE including maladaptive affective behaviors. By contrast, dietary SFN, which targets

Downloaded from https://www.science.org on August 04, 2026

astrocyte redox dyshomeostasis, is effective in normalizing maladaptive affective behaviors but not seizures. Although there are challenges to modeling human mood in rodents, the effectiveness of SFN in normalizing two prelimbic-associated maladaptive affective behaviors suggests its potential translational relevance. SFN is a promising lead compound because it is a brain-penetrant, naturally occurring chemical safely tolerated in humans, already in clinical trials for psychiatric disorders including mood disorders and autism spectrum disorder (*92*–*96*). However, mechanism-driven trials of SFN are still pending (*97*, *98*). In parallel to pursuing the translational potential of SFN itself, further mechanism-driven drug screening using SFN as a lead compound will also be important to establish novel therapeutic strategies. This study may therefore serve as a starting point for mechanism-driven treatment of psychiatric symptoms in PDE that are dissociable from seizures, and a model for uncovering the pathophysiology of psychiatric comorbidities in other epilepsy cases. To extend beyond PDE, future studies should incorporate astrocyte-associated biomarkers including GSH, prefrontal activity patterns, and assays of extracellular [$K^+$]. Our data show that this pathway of astrocyte-elicited maladaptive affective behaviors is reversible, highlighting a broadly addressable astrocyte-driven pathway that can modulate maladaptive affective behaviors independent of seizures, a principle that extends beyond PDE.

## MATERIALS AND METHODS

### Experimental design

Unless otherwise specified, experiments were performed in adult mice 10 to 16 weeks of age. All animals were healthy and were not immune compromised. Expression analyses were performed in C57BL/6NTac mice (RRID:IMSR_TAC:B6). Ibotenic acid and postnatal astrocyte labeling by electroporation (PALE) experiments were performed in C57BL/6J mice (RRID:IMSR_JAX:000664). *Aldh7a1*$^{flox/flox}$ mice (*Aldh7a1*$^{tm1.1Asaw}$; RRID: MGI:8321886) were generated and maintained on a C57BL/6NTac background (see the "Generation of *Aldh7a1* floxed mice" section below). All additional transgenic lines were obtained on a C57BL/6 background and crossed with *Aldh7a1*$^{flox/flox}$ mice for at least two generations. Generation and genotyping of *CMV*$^{Cre}$ (RRID:IMSR_JAX:006054) (*99*), BAC-*Slc1a3*$^{CreER}$ (RRID:IMSR_JAX:012586) (*100*), *Slc1a3*$^{CreER}$ (RRID: MGI:3830051) (*101*), *Emx1*$^{Cre}$ (RRID:IMSR_JAX:005628) (*43*), *Alb1*$^{Cre}$ (RRID:IMSR_JAX:003574) (*102*), *R26*$^{lsl\text{-}mGCaMP3}$ (RRID:IMSR_JAX:030170) (*49*), and *Slc1a2*$^{EGFP}$ (RRID: MGI:5319547) (*103*) have been previously described. To generate KO$^{Global}$ mice, *Aldh7a1*$^{flox/flox}$ mice were crossed with *CMV-Cre* mice and offspring were interbred to obtain *Aldh7a1*$^{-/-}$ mice (*Aldh7a1*$^{tm1.2Asaw}$; RRID: MGI:8321906) lacking *CMV-Cre* (KO$^{Global}$ mice). *Aldh7a1*$^{flox/flox}$ mice were crossed with *Slc1a3*$^{CreER/+}$ mice to generate cKO$^{Astro}$ mice. *Aldh7a1*$^{flox/flox}$ mice were crossed with *Emx1*$^{Cre}$ mice to generate cKO$^{Emx1}$ mice. *Aldh7a1*$^{flox/flox}$ mice were crossed with *Alb1*$^{Cre}$ mice to generate cKO$^{Liver}$ mice. *Aldh7a1*$^{flox/flox}$ mice were crossed with BAC-*Slc1a3*$^{CreER}$ mice to generate cKO$^{Astro(Mosaic)}$ mice. Experimental cKO$^{Astro(Mosaic)}$ and cKO$^{Astro}$ mice were injected with 4-hydroxytamoxifen (4-OHT) (see the "Tamoxifen injections" section below) for induction of the Cre-loxP system from P3-P4 before sexing and genotyping. Genotyping was performed before weaning and reconfirmed postmortem. For cKO$^{Astro}$ and cKO$^{Liver}$ mice, tamoxifen-injected *Aldh7a1*$^{flox/flox}$ Cre-negative littermates were used as controls (Con$^{Astro}$ and Con$^{Liver}$). Both male and female mice were used for experiments to assess astrocyte function in KO$^{Global}$, cKO$^{Astro(Mosaic)}$, and cKO$^{Astro}$ mice using immunofluorescence, biochemical assays, the mito-Grx1-roGFP2 ratiometric sensor, astrocyte calcium imaging, and neuronal calcium imaging in mice injected with astrocyte-targeting AAVs. Male mice were used for transcriptomic, electrophysiological, neuronal calcium imaging in mice treated with SFN and behavioral experiments using the KO$^{Global}$, cKO$^{Emx1}$, cKO$^{Astro}$, cKO$^{Liver}$, and ibotenic acid models. Animals were group housed after weaning and maintained on a 12-hour light/12-hour dark cycle with food and water provided ad libitum. For studies involving the pyridoxine diet or the SFN diet (see the Pyridoxine supplementation and SFN supplementation sections below), cages were randomly assigned to receive standard diet or the experimental diet (pyridoxine or SFN). With the exception of behavioral studies, animals were never involved in previous procedures or studies. For behavioral experiments, animals were sequentially tested on the open field test, FST, and/or the seizure threshold test. Sucrose splash test behavior was assessed in separate cohorts of mice. All animal experiments were approved by and performed in accordance with the Johns Hopkins University School of Medicine Institutional Animal Care and Use Committee (IACUC) and followed National Institutes of Health (NIH) guidelines for proper animal use and welfare.

### Generation of *Aldh7a1* floxed mice

*Aldh7a1* floxed mice containing a *loxP*-flanked allele of *Aldh7a1* were produced by Taconic Biosciences. The targeting strategy was based on the NM_138600.4 transcript. The targeting vector contained *loxP* sites located in nonconserved regions flanking an ~2-kb genomic region containing exons 4 and 5 of the *Aldh7a1* gene. Positive selection markers flanked by FRT [neomycin resistance (NeoR)] and F3 [puromycin resistance (PuroR)] sites were inserted into intron 3 and intron 5, respectively. The targeting vector was generated using BAC clones from the C57BL/6J RPCIB-731 BAC library and transfected into the C57BL/6J ES cell line. Homologous recombinant clones were isolated by double positive selection. Flp-mediated removal of the selection cassettes generated the *Aldh7a1* floxed allele, *Aldh7a1*$^{tm1.1Asaw}$ (MGI:8321886). Cre mediated recombination of the *Aldh7a1* floxed allele deletes exons 4 and 5 and generates a frameshift from exon 3 to exons 6 to 11 resulting in a premature stop codon in exon 6. Germline deletion of the *Aldh7a1* floxed allele generated the null allele *Aldh7a1*$^{tm1.2Asaw}$ (MGI:8321906).

### Genotyping of *Aldh7a1* floxed mice

Routine genotyping of *Aldh7a1*$^{flox}$, *Aldh7a1*$^{+}$, and *Aldh7a1*$^{-}$ alleles was performed by PCR using the following primers at a 2:1:1 ratio: 5′-TCATAGCAGAGCACCTGATACC-3′, 5′-AAAGGCTTTGCACCACTGTG-3′, and 5′-CCTATTGTGAGGGACTTTACCC-3′. These primers amplify a 177–base pair (bp) DNA fragment for the WT allele, a 396-bp fragment for the floxed allele, and a 303-bp fragment for the KO allele. Gels were visualized using Quantity-One software (Bio-Rad).

### Tamoxifen injections

Recombinant deletion of floxed alleles in CreER mouse lines was induced by 2 days of subcutaneous injection of 0.2 mg of 4-OHT (Sigma-Aldrich, H7904, St. Louis, MO, USA), once per day at P3 and P4. 4-OHT was dissolved in ethanol at 20 mg/ml by sonication for long-term storage at −80°C. On the day of injection, 4-OHT/ethanol solution was added to corn oil (1:5 ratio), vortexed for 4 min, and spun on a SpeedVac for 30 min to evaporate the ethanol before injection.

Downloaded from https://www.science.org on August 04, 2026

### Immunofluorescence

According to established protocols (*104*, *105*), mice were perfused with 1X tris-buffered saline (TBS) or phosphate-buffered saline (PBS) followed by 4% paraformaldehyde (PFA); brains were removed and postfixed in 4% PFA overnight.

For immunofluorescence analysis of ALDH7A1 expression, brain sections (30 to 40 μm) were collected using a vibratome or embedded in OCT compound with 7.5% sucrose after incubating in 30% sucrose and collected using a cryostat. Antigen retrieval was performed by incubation with L.A.B. solution (Polysciences Inc.) when necessary: 10 min for 30-μm sections, 25 min for 100-μm sections, and 1 hour for 250-μm sections. Sections were permeabilized in TBS supplemented with 0.3% Triton X-100, blocked in 5% serum overnight at 4°C with primary antibody, washed in TBS, incubated with Alexa Fluor–conjugated secondary antibody + 4′,6-diamidino-2-phenylindole (DAPI) for 2 hours at room temperature (RT), washed, and mounted on Superfrost Plus slides using ProLong Gold Antifade reagent.

For immunolabeling of acute brain slices used for astrocyte microdomain $Ca^{2+}$ imaging experiments, sections were incubated in primary antibody for ~40 hours at 4°C followed by ~16 hours in secondary antibody at 4°C and mounted with Vectashield mounting media with DAPI (Vector Labs H-1200).

For immunofluorescence analysis of NRF2, c-FOS, and MAP2, antigen retrieval was performed on 40-μm-thick sections by preincubating in 1× Tris-EDTA (pH 9.0) (Abcam) at 80°C for 40 min [NRF2, c-FOS] or HistoVT One (Nacalai, 06380-05) at 65° to 70°C for 30 min [MAP2]. Sections were then permeabilized in PBS supplemented with 0.5% Triton X-100 and blocked for 1 hour in 10% serum. Subsequently, sections were incubated overnight at 4°C with Alexa Fluor–conjugated primary antibodies. After incubation, sections were washed in PBS containing DAPI and mounted on Superfrost Plus slides using ProLong Gold Antifade reagent. Immunofluorescence analysis was performed in the same way for tissue from mice with stereotactic injection of AAVs for neuronal $Ca^{2+}$ imaging.

#### *Antibodies used*

The antibodies used in this study were as follows: rabbit anti-ALDH7A1 EP1935Y (Abcam, 53278; RRID:AB_867570; 1:250), chicken anti-GFP (Abcam, 13970; RRID:AB_300798; 1:2000), mouse anti-ALDH1L1 (Millipore, MABN495; RRID:AB_2687399; 1:1000), mouse anti-CC1 (Calbiochem, OP80; RRID:AB_2057371; 1:50), guinea pig anti-NG2 (William Stallcup, Burnham Institute; RRID:AB_2572299; 1:1000), goat anti-IBA1 (Novus, NB100-1028; RRID:AB_3148646; 1:250), mouse anti-NeuN (Millipore, MAB377; RRID:AB_2298772; 1:500), mouse anti-GFAP (Millipore, MAB360; RRID:AB_11212597; 1:400), mouse anti-8-oxo-dG (Trevigen, 4354-MC-050; RRID: AB_1857195; 1:250), rabbit anti-NRF2-Alexa Fluor 488 (Abcam, 194984; RRID:AB_2889229; 1:100), anti-NRF2-Alexa Fluor 647 (Abcam, 194985; RRID:AB_3740753; 1:100), rabbit anti-ALDH1L1/2-Alexa Fluor 568 (Abcam, 313067; RRID: AB_3741584; 1:100), rat anti-GFP (Nacalai Tesque, 04404-84; RRID:AB_10013361; 1:1000), rabbit anti-mCherry (Cell Signaling Technology, 43590; RRID: AB_2799246; 1:500), mouse anti-mCherry (Proteintech, 68088-1-Ig; RRID:AB_2918825; 1:400), rat anti-RFP (ChromoTek, 5f8; RRID: AB_2336064; 1:1000), rabbit anti-NeuN (Cell Signaling Technology, 12943; RRID:AB_2630395; 1:250), and secondary antibodies conjugated with Alexa Fluor 405, Alexa Fluor 488, Alexa Fluor 568, and Alexa Fluor 647.

#### *Imaging and analysis*

Immunofluorescence images were collected on Zeiss 800 and Zeiss 880 confocal microscopes using the ZEN Blue/Black software.

For ALDH7A1 expression analysis, we collected *z*-stacks at 20x in three fields of view (FOVs) per mouse in the prelimbic cortex and, for each cell type marker, counted the percentage cells that coexpressed ALDH7A1. Representative tiled images were acquired with 10x objective lens.

For anti-NRF2 analysis, we collected single *z*-plane confocal images at 40x in three FOVs per mouse from the prelimbic cortex. Quantification of anti-NRF2 fluorescence intensity in astrocytes and nonastrocyte regions was performed using the FIJI software. Images were manually thresholded using the ALDH1L1 channel to identify astrocyte cell bodies, and the mean fluorescence intensity was measured both within the ALDH1L1-positive region (astrocytes) and the ALDH1L1-negative region (nonastrocytes).

### Immunohistochemistry with DAB development

After fixation, the heart, lung, liver, kidney, and small intestine were processed, embedded in paraffin, and cut at 10 μm in thickness. Deparaffinization and antigen retrieval were done in Dewax and HIER buffer M (Richard-Allen Scientific LLC, TA-999-DHBM) at 97°C for 20 min on PT Module (Thermo Fisher Scientific, A80400012). Staining steps by 3,3′-diaminobenzidine (DAB) development were performed on Lab Vision Autostainer 360 (Thermo Fisher Scientific, A80500024). The tissues were incubated in 3% hydrogen peroxidase solution for 15 min at RT. After washing with TBS, samples were blocked in TBS with 5% normal goat serum for 1 hour at RT. ALDH7A1 antibody (Abcam, ab53278) was incubated in blocking buffer for 1 hour at RT. Samples were washed three times in PBS for 5 min, and then biotinylated anti-rabbit IgG (H + L) (Vector Labs, BA-1100) in TBS was applied and incubated for 1 hour at RT. Samples were washed three times in TBS, and the ABC reagent prepared as instructed by the manufacturer was applied and incubated for 1 hour at RT. Samples were washed three times in TBS, and DAB (Vector Labs, SK-4100) solution was applied and incubated for 3 min at RT as instructed by the manufacturer. The color-developed samples were counterstained with hematoxylin (Thermo Fisher Scientific, 7211). After dehydration and serial incubation in xylene, samples were coverslipped. Images were taken by an Olympus BX51TF with a DP70 color camera in the Microscope Facility of the Johns Hopkins School of Medicine or by Canon EOS 50D.

### Western blotting

Cortical tissue samples were obtained from adult mice following cervical dislocation and cortical dissection, snap frozen in liquid nitrogen, and stored at −80°C. "Rest of brain" samples in which the cortices and cerebellum had been removed were also collected in some cases. Protein lysates were prepared by homogenization in lysis buffer (radioimmunoprecipitation assay + protease inhibitors; Roche). For Western blotting, 20 μl of the sample containing 20 μg of the total protein was added to each lane of a Novex 8% Tris-Glycine gel (Life Technologies) and run at 100 V at RT followed by transfer to a polyvinylidene difluoride membrane at 4°C. Membranes were blocked for 1 hour in 5% milk in PBS and 1% Tween 20, incubated in primary antibody overnight, washed in PBS and Tween, incubated in secondary antibody (anti-mouse or anti-rabbit HRP; GE Healthcare) for 1 hour at RT, washed in PBS and Tween, incubated with enhanced chemiluminescent substrate (ECL, Pierce), exposed, and

Downloaded from https://www.science.org on August 04, 2026

quantified using an ImageQuant LAS 4000 mini (GE) digital image acquisition system. Raw images were quantified in ImageJ. Rectangular regions of interest (ROIs) were drawn around selected bands, and mean gray value was reported by the measure tool. In each experiment, the same size ROI was used for all bands for every antibody. Background signal was measured by moving the ROI to an empty area of the blot and subtracted from the target signal before normalization to loading control signal. Blots were cropped, and in some cases, levels were adjusted for figure clarity. In these cases, image processing was always uniformly applied to all bands for each antibody. Experimenters were blind to the identity of the samples until analysis was complete. Antibodies used were as follows: rabbit anti-ALDH7A1 EP1934Y (Abcam, 68192; RRID: AB_3741586; 1:5000), mouse anti-ALDH1L1 (Millipore, MABN495; RRID:AB_2687399; 1:1000), and mouse anti-GAPDH (Santa Cruz, sc-32233; RRID:AB_627679; 1:10,000).

## Animal behavior

According to established protocols (*106*, *107*), behavioral testing was performed in cohorts of 8 to 15 male mice starting at 10 to 14 weeks of age with tests in the following order: open field test, FST, and seizure threshold test. Sucrose splash test behavior was assessed in separate cohorts of mice. Experiments were performed at RT. Experimenters were blind to the genotype of the animals during testing and video analysis of the behaviors. Stopwatch+ (Center for Behavioral Neuroscience, Atlanta, GA) was used for video analysis of the FST and seizure threshold test. Grooming events were counted using https://spacebarclicker.org/ (*108*).

### *Open field test*

Open field locomotor activity was measured for 120 min in a novel open field box (40 cm by 40 cm; San Diego Instruments, San Diego, CA). Horizontal and vertical locomotor activities were automatically recorded by an infrared activity monitor (San Diego Instruments). Single beam breaks were analyzed within 10-min bins and are reported as "counts."

### *Forced swim test*

Forced swim response was measured by placing the mice in a 5000-ml glass beaker half-filled with water. We quantified the percentage of time the mice were actively swimming during the first 2 min.

### *Sucrose splash test*

The sucrose splash test was conducted according to established protocols by applying a 10% sucrose solution to the dorsal coat of each mouse within its home cage (*38*). The viscous nature of the sucrose solution ensures its adherence to the mouse fur, thereby eliciting grooming. Following the application of sucrose, two parameters were manually recorded in a blinded manner over a 5-min observation period: the latency to initiate grooming and the frequency of grooming events. Self-grooming was specifically defined as licking of the fur or stroking and scratching of the face and body. These measures served as indices of self-care and motivational behavior.

### *Seizure threshold test*

Each mouse was weighed, administered a series of three doses of PTZ at 30 min intervals [30, 30, and 60, intraperitoneally (ip); Sigma-Aldrich, P6500], and monitored until 30 min following the last dose. Seizure severity was scored on a modified Racine scale (*109*, *110*), and the median effective concentration ($EC_{50}$) of the dose-response curve was estimated by a nonlinear least-squares regression model.

## Pyridoxine supplementation

Mouse chow containing pyridoxine (125 mg/kg; catalog no. D16032903) or a standard diet (open standard diet; catalog no. D11112201) was obtained from Research Diets (New Brunswick, NJ). $KO^{Global}$ mice were fed either pyridoxine-supplemented chow or standard chow starting 14 days before behavioral experiments. The food in the cage feeder was replaced every 7 days with fresh chow that had been stored at 4°C or colder. Each time the food was changed, 21 g of diet was added to each cage for every mouse housed in it.

## RNA-seq of cortical tissue

Cortical tissue was dissected from $KO^{Global}$ mice, and RNA was extracted using the RNeasy kit (Qiagen). Total RNA was assessed for quality via the Agilent Bioanalyzer and Thermo Fisher Scientific NanoDrop, and RNA libraries were prepared using the Illumina TruSeq Stranded RNA LT Kit with Ribo-Zero Gold rRNA depletion. Barcoded libraries were quality controlled using the Kappa PCR kit and pooled in equimolar ratios for subsequent cluster generation and sequencing on an Illumina HiSeq 2000 instrument to yield >50,000,000 paired end 100x100-bp tags for each sample.

### *Preprocessing and aligning RNA-seq reads to reference genome*

FastQC (*111*) was used to check the quality of reads. Reads were aligned to the mouse genome (mm10) using STAR (*112*) with the following optional parameters: --runThreadN 8 --outSAMtype BAM SortedByCoordinate --quantMode GeneCounts. Count from the ReadsPerGene table generated from STAR was used for further analysis.

### *Differential gene expression analysis*

Normalization and differential expression analysis were performed using the R package deseq2 (*113*). Genes with false discovery rate (FDR) smaller than 0.05 were identified as differentially expressed genes (DEGs).

### *Pathway analysis*

We performed GSEA (*114*) on Gene Ontology (GO) biological processes and molecular function terms to identify overrepresented pathways. All genes, including DEGs and non-DEGs, ranked by statistical significance obtained from differential expression analysis were used as the query list. The GSEAPreranked module was used for the analysis. Pathways with less than 5 genes or more than 1000 genes were excluded (options -set_max 1000 -set_min 5). Pathways with an FDR smaller than 0.05 were identified as significantly overrepresented sets.

### *Network visualization*

Gene sets of interest were loaded into Cytoscape for visualization. The EnrichmentMap plug-in (*45*) was used to identify gene sets with overlapping genes. The AutoAnnotate plug-in was used to group gene sets with overlapping genes into biological themes. Biological themes were manually labeled to reflect the common function of the gene sets within that biological theme.

## Redox biochemical assays

Levels of $NAD^+$/NADH, $NADP^+$/NADPH, and GSH/GSSG were measured using commercial kits following the manufacturer's instructions.

### *$NAD^+$/NADH*

$NAD^+$/NADH was measured using a colorimetric assay kit (K337-100, BioVision Inc., Melpitas, CA). Mouse brains were harvested, washed in PBS, and the cortex was isolated. Tissue samples (~20 mg) were homogenized and sonicated in extraction buffer, centrifuged at

Downloaded from https://www.science.org on August 04, 2026

14,000 rpm for 5 min at 4°C, and filtered through 10-kDa molecular weight cutoff filters (catalog no. 1997, BioVision). Two hundred microliters of each sample was heated at 60°C for 30 min to degrade $NAD^+$ and then cooled on ice. Fifty microliters of the degraded sample, 50 μl of the undegraded sample, and 50 μl of NADH standards were loaded into a 96-well plate, mixed with NAD cycling reagent to convert the remaining $NAD^+$ to NADH, incubated at RT for 5 min, mixed with NADH developer, and incubated at RT for 2 hours. The amount of NADH was determined using endpoint measurement of absorbance at 450 nm and comparing to the standard curve. Measurements from the degraded samples reflected levels of NADH, whereas measurements from undegraded samples reflected the total combined level of $NAD^+$ and NADH. $NAD^+$ levels were determined by subtracting NADH levels from the combined level of $NAD^+$ and NADH and then used to compute the $NAD^+$/NADH ratio.

***$NADP^+$/NADPH***

$NADP^+$/NADPH levels were measured using a fluorometric assay kit (MET-5031 Cell Biolabs Inc.). Mouse brains were perfused with cold PBS, and the prefrontal cortex (PFC) was isolated by coronally cutting the brain at the optic chiasm, removing the olfactory bulbs, and extracting the portion of the cerebral cortex anterior to the optic chiasm. Tissue samples (100 mg) were homogenized and sonicated in extraction buffer and then centrifuged at 14,000 rpm for 5 min at 4°C. The supernatant was filtered using a 10-kDa spin filter to remove proteins, and the flow-through was collected for analysis and stored at −80°C. For NADPH measurement, samples were treated with NaOH, incubated at 80°C for 60 min, neutralized with assay buffer, vortexed, and centrifuged. $NADP^+$ measurement followed a similar procedure using HCl. Samples and standards (50 μl) were loaded into a 96-well plate, mixed with NADP cycling reagent, and incubated for 1 to 2 hours at RT. Fluorescence was measured at an excitation of 530 to 570 nm and an emission of 590 to 600 nm. NADP+/NADPH concentrations were determined using a standard curve.

***GSH/GSSG***

GSH/GSSG levels were measured using a colorimetric Glutathione Assay Kit (Cayman Chemical, #703002, Ann Arbor, MI). Mouse brains were perfused with cold PBS, and the PFC was isolated by coronally cutting the brain at the optic chiasm, removing the olfactory bulbs, and extracting the portion of the cerebral cortex anterior to the optic chiasm. Tissue samples (100 mg) were homogenized and sonicated in cold MES buffer and then centrifuged at 10,000*g* for 15 min at 4°C. The supernatant was removed and deproteinated. Metaphosphoric acid (MPA) reagent was prepared by dissolving 5 g of MPA in 50 ml of water. Equal volumes of MPA reagent were added to samples, vortexed, incubated at RT for 5 min, and centrifuged at >2000*g* for at least 2 min. The supernatant was carefully collected, avoiding disturbance of the precipitate. Homogenized samples were diluted to 1/10 and 1/100 using half-diluted MES buffer with MPA reagent. A 1 M solution of 2-vinylpyridine in ethanol was prepared. Ten microliters of this solution was added per milliliter of deproteinated sample, vortexed, incubated at RT for 60 min, and assayed. For the assay, 50 μl of the standard and 50 μl of the sample were added to each well of a 96-well plate. The plate was covered, and an assay cocktail was prepared by mixing MES buffer, reconstituted cofactor mixture, reconstituted enzyme mixture, and water. After removing the plate cover, 150 μl of freshly prepared assay cocktail was added to each well, and the plate was incubated in the dark on an orbital shaker. GSH concentration was determined using the endpoint method, measuring absorbance at 405 to 414 nm after 25 min.

### Cloning and generation of AAVs

All cloning was performed using the Gibson Assembly method. pLPCX mito Grx1-roGFP2 was a gift from T. Dick (Addgene, plasmid #64977), pZac2.1 gfaABC1D-tdTomato was a gift from B. Khakh (Addgene, plasmid #44332), pAAV-CaMKIIa-mCherry was a gift from K. Deisseroth (Addgene, plasmid #114469), and AAV-CMV-Nrf2 was a gift from C. Cepko (Addgene, plasmid #67636). The pZac2.1 GfaABC1D-mito-Grx1-roGFP2 plasmid was generated by cloning the mito-Grx1-roGFP2 coding sequence from pLPCX mito Grx1-roGFP2 into the pZac2.1 gfaABC1D-tdTomato vector. The pZac2.1-GfaABC1D-mCherry plasmid was generated by replacing the tdTomato sequence from pZac2.1 GfaABC1D-tdTomato with the mCherry sequence from pAAV-CaMKIIa-mCherry. The pZac2.1-GfaABC1D-ALDH7A1-mCherry plasmid was generated by inserting the mouse ALDH7A1 CDS (NCBI RefSeq: NM_138600.4) into the pZac2.1 GfaABC1D-mCherry plasmid. The pZac2.1-GfaABC1D-Nrf2-mCherry plasmid was generated by replacing the ALDH7A1 CDS in pZac2.1-GfaABC1D-ALDH7A1-mCherry with the *Nrf2* CDS from AAV-CMV-Nrf2. pGfaABC1D-mCherry-*Keap1*-shRNA and pGfaABC1D-mCherry-scramble-shRNA were generated by inserting a *Keap1* shRNA sequence (5′-CCTGCAACTCGGTGATCAATTC-3′) or a nontargeting scrambled shRNA sequence (5′-GGCTCCCGCTGAATTGGAATCC-3′) into a pAAV (AAV2 ITR–based) transfer backbone containing a pUC/ColE1 origin, ampicillin resistance, and WPRE. The *Keap1* shRNA sequence was designed and embedded in an miR-30 backbone using VectorBuilder (https://en.vectorbuilder.com/) based on a validated small interfering RNA (siRNA) sequence (*115*). The sequences for all newly generated plasmids were deposited in GenBank under the following accession numbers: pZac2.1-GfaABC1D-mCherry (PZ285974), pZac2.1-GfaABC1D-ALDH7A1-mCherry (PZ285975), pZac2.1-GfaABC1D-mito-Grx1-roGFP2 (PZ285976), pZac2.1-GfaABC1D-Nrf2-mCherry (PZ285977), pGfaABC1D-mCherry-scramble-shRNA (PZ285978), and pGfaABC1D-mCherry-*Keap1*-shRNA (PZ285979). AAV5 viral particles were packaged at $1 \times 10^{13}$ genome copies (GC)/ml by Applied Biological Materials Inc. (Richmond, BC, Canada).

### Assessment of astrocyte redox using the mito-Grx1-roGFP2 ratiometric sensor

AAV5-GfaABC1D-mito-Grx1-roGFP2 was bilaterally injected in the prelimbic cortex by stereotax [anteroposterior (AP): +1.94, mediolateral (ML): ±0.3, and dorsoventral (DV): −1.5] to express mito-Grx1-roGFP2 in astrocytes. Following established protocols (*116*), mice were perfused 4 weeks after AAV injection with PBS containing 50 mM *N*-ethylmaleimide (NEM), followed by 4% PFA with 50 mM NEM. The extracted brains were then immersed in 4% PFA with 50 mM NEM overnight. Subsequently, brains were sectioned into 40-μm-thick slices using a vibratome (Leica VT1200S). Sections were treated with 0.5% Triton X-100 in PBS containing 1 mM TO-PRO-3 (Thermo Fisher Scientific, #T3605) for 20 min, followed by three washes in PBS. Last, sections were mounted on Superfrost Plus slides using ProLong Gold Antifade reagent. Fluorescence images were acquired frame by frame using a Zeiss LSM800 confocal microscope. Emission was collected from 500 to 700 nm, with sequential excitation provided by 405- and 488-nm laser lines. For each brain slice, a minimum of two images were captured using a 63x objective. Raw image data from the 405- and 488-nm laser lines were exported as 16-bit TIFF files for subsequent analysis with the ImageJ software. To remove background fluorescence pixels, lower thresholds were

Downloaded from https://www.science.org on August 04, 2026

applied to the 488-nm images. After defining selections based on these thresholds, the signal intensities for both the 488- and 405-nm images were measured.

### Astrocyte acute slice calcium imaging

Astrocyte calcium signals from acute brain slices containing the prelimbic cortex were prepared, acquired, and analyzed using the CasCaDe MATLAB code as previously described (*49*). Mice were deeply anesthetized with isoflurane and decapitated using a guillotine. Their brains were dissected out and mounted on a vibratome (Leica VT100S) equipped with a sapphire blade. Cortical slices (250 μm in thickness) were cut in ice-cold *N*-methyl-D-glucamine (NMDG)–based cutting solution containing 135 mM NMDG, 1 mM KCl, 1.2 mM $KH_2PO_4$, 1.5 mM $MgCl_2$, 0.5 mM $CaCl_2$, 10 mM dextrose, and 20 mM choline bicarbonate (pH 7.4). Cortical slices were then transferred to artificial cerebral spinal fluid (ACSF) containing 119 mM NaCl, 2.5 mM KCl, 2.5 mM $CaCl_2$, 1.3 mM $MgCl_2$, 1 mM $NaH_2PO_4$, 26.2 mM $NaHCO_3$, and 11 mM dextrose (292 to 298 mosmol/liter) and were maintained at 37°C for 40 min and at RT thereafter. Both NMDG solution and ACSF were bubbled continuously with 95% $O_2$/5% $CO_2$. All slice imaging experiments were performed at RT. Fluorescence changes arising from mGCaMP3 were recorded from individual cortical astrocytes using a Zeiss LSM 710 microscope with a 20x (numerical aperture: 1.0) water immersion objective (Zeiss), using the 488-nm laser line. $GCaMP3^+$ astrocytes with no $GCaMP3^+$ neighbors were selected for imaging in at least three cortical sections from four separate mice. Only one cell was imaged in each slice. Slices were continuously superfused with ACSF bubbled with 95% $O_2$/5% $CO_2$. Astrocytes were imaged at a laser power of 29 μW, with no pixel averaging, high photomultiplier tube gain (~800), and with a pinhole size of 2.69 airy units, corresponding to 3.6 μm of *z*-depth. For each experimental session, individual astrocytes (~3500 to 4900 $\mu m^2$) contained within the prelimbic cortex were imaged at the pixel depth of 8 bit with a resolution of 512 × 512 pixels. Individual imaging sessions consisted of 600 frames at a frame scan rate of 2.1 Hz (0.484 s/frame). Each imaging session consisted of 5-min imaging to control for photoactivation before baseline measurements, 5-min baseline measurements, 15-min bath application of 200 nmol of tBHP (Luperox 458139, Sigma-Aldrich) to induce ROS, and 5-min imaging after tBHP application. To compensate for minor drift in the *XY* plane, image stacks were post hoc registered using TurboReg (plug-in for ImageJ) for automatic alignment of images. Astrocytes located on the surface of the slice, those that had large blood vessels passing through them, or exhibited image registration artifacts were excluded from the dataset. Following imaging, the relative position of the cell in the section was recorded and a low-magnification image was taken to allow the cell to be mapped during post hoc immunohistochemistry by morphology, laser position, and the relative positions of nearby $GCaMP3^+$ cells. We used the CasCaDe algorithm to identify and extract kinetic information about individual microdomain activity as previously described (*49*). Experimenters were blinded to the expression of ALDH7A1 in each astrocyte during imaging and analysis.

### Flow cytometry

For flow cytometry experiments, $KO^{Global}$ mice were interbred with $Slc1a2^{EGFP/+}$ (*103*) mice, which express enhanced green fluorescent protein (EGFP) in all astrocytes. On each day of analysis, we analyzed one $KO^{Global}$; $Slc1a2^{EGFP/+}$ and one $Slc1a2^{EGFP/+}$ littermate control. Cortices were dissected, separated from the hippocampus, and dissociated with a papain-based neural tissue dissociation kit (Milenyi Biotec) to obtain a single-cell suspension. After incubation, cell suspensions were spun down, the supernatant was removed, and cells were resuspended in neurobasal media supplemented by 1% bovine serum albumin (BSA). For measurement of ROS, 1 μL of CellROX Deep Red reagent was added to samples containing 500,000 cells in 1 ml and incubated at 37°C for 30 min. Samples were then run on a MoFlo Legacy (Beckman Coulter) flow cytometer to analyze levels of CellROX fluorescence intensity in each cell population. Astrocytes were identified on the basis of the expression of EGFP. Single color controls were used for compensation. Propidium iodide was added to the samples to exclude dead cells. The mean fluorescence intensity was calculated using the FlowJo software. The fold change in mean fluorescence intensity between $KO^{Global}$; $Slc1a2^{EGFP/+}$ and one $Slc1a2^{EGFP/+}$ astrocytes was calculated for each day of analysis.

### Mitochondrial stress test

Primary cortical astrocyte cultures were prepared from litters of $Aldh7a1^{-/-}$ pups and $Aldh7a1^{+/+}$ pups between P5 and P9 of age on the C57BL/6NTac background. Litters contained both sexes, and cells from each litter were pooled. Cortices were dissected, separated from the hippocampus, and dissociated with a papain-based neural tissue dissociation kit (Miltenyi Biotec). Astrocytes were purified by magnetic-activated cell sorting (MACS) technology using $ACSA2^+$ microbeads (Miltenyi Biotec). Cells were grown in T-75 flasks precoated with poly-L-lysine (15 μg/ml; Sciencell) in Dulbecco's modified Eagle's medium (DMEM)/F-12 supplemented with 15% fetal bovine serum and 1% penicillin/streptavidin and incubated at 37°C in 5% $CO_2$. After 14 days in vitro (DIV), cells were replated in a 24-well dish at 40,000 cells per well. Experiments were performed 2 days after replating.

Measurements of oxygen consumption rate (OCR) in primary astrocytes were performed on a Seahorse XF24 Extracellular Flux analyzer (Seahorse Bioscience). Two days before the assay, primary astrocytes were seeded into XF24 24-well microplates. The day before the assay, the cells were then placed in a 37°C incubator without $CO_2$. In addition, an XF sensor cartridge was hydrated with Seahorse Bioscience Calibrant in an XF Utility plate and placed in a 37°C $CO_2$-free incubator overnight for 12 hours. The day of the assay, $CO_2$-free Seahorse Base Media was combined with 10 mM glucose, 1 mM sodium pyruvate, and 1x GlutaMAX (Thermo Fisher Scientific) and brought to pH 7.4. The cells were washed with this media and incubated in it for 1 hour in the $CO_2$-free incubator. During this incubation, the hydrated cartridge was loaded with oligomycin (1 μM), carbonyl cyanide *p*-trifluoromethoxyphenylhydrazone (2 μM), and antimycin A (0.5 μM) and rotenone (0.5 μM). The loaded cartridge was placed onto the cell well plate and inserted into the XF24 analyzer for repeated measurement of OCR and extracellular acidification rate (ECAR) at baseline and after sequential application of the mitochondrial blockers to assess mitochondrial basal respiration, ATP production, maximal respiration capacity, and spare capacity. Measurement cycles consisted of 3-min mix, 2-min wait, and 3-min measure. Empty cells spaced throughout the plate are used as negative controls. These experiments were also repeated with application of 200 μM TBHP after baseline measurements to determine the effect of TBHP on cellular metabolism.

Downloaded from https://www.science.org on August 04, 2026

### SFN supplementation

Mouse chow containing 600 parts per million D,L-SFN (catalog no. D15102501) or a standard diet (open standard diet; catalog no. D11112201) was obtained from Research Diets (New Brunswick, NJ). The D,L-SFN used for the diet was sourced from Toronto Research Chemicals (Toronto). Unless otherwise specified, treated mice and littermate controls were placed on an SFN supplemented diet or a standard diet at the time of weaning, at 3 weeks of age. Cages of KO mice and control littermates were randomly assigned to receive the SFN diet or the standard diet. The food in the cage feeder was replaced every 7 days with fresh chow that had been stored at 4°C or colder. Each time the food was changed, 21 g of diet was added to each cage for every mouse housed in it.

### Measurement of SFN in chow

Pellets stored at either 4° or ~23°C for 0, 6, 14, or 42 days were comminuted into fine powder using a small Krups coffee mill and extracted into 10 volumes of a chilled mixture of equal parts of water, acetonitrile, *N*,*N*′-dimethylformamide, and dimethyl sulfoxide. SFN was measured in these extracts by two separate methods, direct chromatography [high-performance liquid chromatography (HPLC)], and cyclocondensation of total isothiocyanates (both free and conjugated SFN in the feed are captured by the latter method). 1,2-Benzenedithiol was purchased from Alfa Aesar (catalog no. L11253) and stored at −20°C. The SFN standard was purchased from LKT Laboratories (catalog no. S8044). The Empower 3 software (Waters) was used for data acquisition.

#### *Direct chromatography*

Extracts were clarified by centrifugation, diluted at least 10-fold in HPLC mobile phase [5% (v/v) tetrahydrofuran in water], and then applied to a C18 reversed-phase Genesis Lightning (4.6 mm by 50 mm, 3-µm HPLC column; Grace Davison Discovery Sciences, catalog no. FM5963E), which was equilibrated with 5% tetrahydrofuran in water and eluted isocratically at 2 ml/min. Elution was monitored at 240 nm (the approximate $\lambda_{max}$ of SFN). The retention time was determined by comparison with an authentic SFN standard purchased from LKT Laboratories.

#### *Cyclocondensation*

Total levels of isothiocyanate equivalents (isothiocyanates plus their metabolites) were measured using the HPLC-based cyclocondensation assay reaction with 1,2-benzenedithiol (*117*, *118*). Isothiocyanates are metabolized to dithiocarbamates in vivo, and the cyclocondensation assay detects both isothiocyanates and dithiocarbamates. Briefly, each 2-ml reaction mixture in a 4-ml glass vial contained 100 mM borate buffer (pH 9.2), and 16.3 mM 1,2-benzenedithiol, in 50% methanol/50% water. The reaction mixture was incubated for 2 hours at 65°C and, after cooling to RT, was centrifuged at low speed to sediment insoluble materials. Aliquots of the supernatant (50- and 100-µl replicates) were analyzed by HPLC, on an ODS C18 Hypersil (100 mm by 4.6 mm, 5-µm column; Thermo Fisher Scientific, #30105-104630). The mobile phase was 80% methanol/20% water, the flow rate was 0.5 ml/min, and the absorbance was monitored at 365 nm as described previously (*117*, *118*).

### Pharmacological lesioning

Pharmacological lesioning was performed by stereotactic injection of ibotenic acid (Sigma-Aldrich, catalog no. I2765), an *N*-methyl-D-aspartate (NMDA) glutamate receptor agonist (*119*). Bilateral injections of 1 µl of ibotenic acid solution (2.5 µg/µl in saline) or vehicle (saline) were performed in either the prelimbic cortex (AP: +1.94, ML: ±0.3, and DV: −1.5) or the cerebellum (AP: −6.4, ML: ±2.7, and DV: −1.5), 4 weeks before behavioral testing.

### Neuronal acute slice calcium imaging and analysis

Calcium imaging experiments in $cKO^{Astro}$ mice and $KO^{Global}$ mice treated with SFN and experiments using ouabain were performed using an epifluorescence microscope. pENN.AAV.CamKII.GCaMP6f.WPRE.SV40 was a gift from J. M. Wilson (Addgene, viral prep #100834-AAV9)

Four weeks before acute slice preparation and imaging, mice were stereotactically injected in the prelimbic cortex (AP: +1.94, ML: ±0.3, and DV −1.5) with AAV9 pENN.AAV.CamKII.GCaMP6f.WPRE.SV40. On the day of imaging, mice were anesthetized with ether and perfused using cold NMDG-based cutting solution containing 135 mM NMDG, 1 mM KCl, 1.2 mM $KH_2PO_4$, 1.5 mM $MgCl_2$, 0.5 mM $CaCl_2$, 10 mM dextrose, and 20 mM choline bicarbonate (pH 7.4) as previously described (*49*). Brains were dissected out and mounted on a vibratome (Leica VT100S). Cortical slices (250 µm in thickness) were cut in ice-cold NMDG-based cutting solution. Cortical slices were then transferred to ACSF containing 119 mM NaCl, 2.5 mM KCl, 2.5 mM $CaCl_2$, 1.3 mM $MgCl_2$, 1 mM $NaH_2PO_4$, 26.2 mM $NaHCO_3$, and 11 mM dextrose (292 to 298 mosmol/liter) and were maintained at 37°C for 40 min and at RT thereafter. Both the NMDG solution and ACSF were bubbled continuously with 95% $O_2$/5% $CO_2$. Experiments were carried out at RT.

Fluorescence dynamics arising from $GCaMP6^+$ excitatory neurons in the prelimbic cortex were recorded using a fixed-stage microscope (BX61-WI, Olympus) with optical lens (40x/0.80 objective, LumPLanFL N), a 300-W Xenon lamp using a GFP filter, high-speed galvo mirror with filters (DG4-1015, Shutter Instrument Company), and infrared-sensitive charge-coupled device camera (iXon3, ANDOR Technology). For each brain section, one FOV in the prelimbic cortex was imaged for 600 frames in ~200 s. Images were processed with the digital imaging software (MetaFluor for Olympus and Metamorph Advanced Molecular Device). All these systems are on an antivibration floating table (Technical Management Corp.) and connected to a PC (Windows 7, Microsoft). For imaging analysis, raw videos were preprocessed by applying ×4 spatial downsampling to reduce the file size and processing time, but no temporal downsampling was applied (*120*). To reliably deal with the large fluctuating background, we applied the CNMFe algorithm (https://github.com/zhoupc/CNMF_E) (*120*) that is a recent adaptation of the CNMF algorithm (*121*), enabling us to identify individual neurons, obtain their fluorescence traces, and deconvolve fluorescence signals into neural activity. To define the initial spatial components, candidate seed pixels were manually selected from peak-to-noise (PNR) graphs of the FOV (*122*). Calcium events with $z$-scores < 8 or those that did not have an area under the curve (AUC) < 0.5 were excluded from analyses because events of this magnitude did not reliably retain transient, calcium event characteristics across animals. All neurons with at least one detected event were used to calculate the mean $Ca^{2+}$ event rate.

For experiments using ouabain, each slice was imaged continuously for 600 s. Ouabain (50 µM; MilliporeSigma, O3125) was added by bath application at 260 s. $Ca^{2+}$ events from 0 to 200 s were analyzed and used determine the baseline $Ca^{2+}$ event rate. $Ca^{2+}$ events from

Downloaded from https://www.science.org on August 04, 2026

400 to 600 s were analyzed and used to determine the $Ca^{2+}$ event rate in the presence of ouabain. All neurons with at least one detected event both at baseline and in the presence of ouabain were used to calculate the mean $Ca^{2+}$ event rate for each slice, both at baseline and in the presence of ouabain. To determine the effect of ouabain on $Ca^{2+}$ event rate in $cKO^{Astro}$ neurons versus $Con^{Astro}$, we performed a repeated-measures two-way analysis of variance (ANOVA).

Calcium imaging experiments in $cKO^{Astro}$ mice with stereotactic injection of AAVs were performed using a spinning disk confocal microscope: Four weeks before acute slice preparation and imaging, mice were stereotactically injected in the prelimbic cortex (AP: +1.94, ML: ±0.3, and DV: −1.5) with AAV9 pENN.AAV.CamKII.GCaMP6f.WPRE.SV40 (Addgene, #100834) coinjected with either AAV5-GfaABC1D-ALDH7A1 (ALDH7A1 Rescue), AAV5-GfaABC1D-mCherry (control AAV), AAV5-GfaABC1D-Nrf2 together with AAV5-GfaABC1D-mCherry-Keap1 shRNA (NRF2 Rescue), or AAV5 pZac2.1-GfaABC1D-mCherry together with AAV5 pGfaABC1D-mCherry-scramble RNA (control scramble AAV). On the day of imaging, mice were anesthetized and perfused as described above. For confocal imaging, cortical slices (300 μm in thickness) were transferred to ACSF. The ACSF for ALDH7A1 Rescue experiments contained 120 mM NaCl, 3.5 mM KCl, 2.5 mM $CaCl_2$, 1.3 mM $MgCl_2$, 1 mM $NaH_2PO_4$, 26.2 mM $NaHCO_3$, and 11 mM dextrose (295 to 305 mosmol/liter). The ACSF for NRF2 Rescue experiments contained 126.0 mM NaCl, 3.5 mM KCl, 1.0 mM $CaCl_2$, 0.5 mM $MgCl_2$, 1.25 mM $NaH_2PO_4$, 10.0 mM dextrose, and 10.0 mM Hepes (295 to 305 mosmol/liter). Otherwise, slices and solutions were maintained as described above.

Confocal imaging of GCaMP6 fluorescence dynamics was performed on a Leica confocal microscope with a Yokogawa Spinning Disk unit (CSU10) for ALDH7A1 Rescue AAV or on a Nikon Eclipse TiE fully motorized inverted confocal microscope with a Yokogawa Spinning Disk unit (CSU10) for NRF2 Rescue AAVs. All these systems were on an antivibration floating table (Technical Management Corp.) and connected to a PC (Windows 11, Microsoft). During imaging, sections were kept in circulating ACSF containing 126.0 mM NaCl, 3.5 mM KCl, 1.0 mM $CaCl_2$, 0.5 mM $MgCl_2$, 1.25 mM $NaH_2PO_4$, 26.0 mM $NaHCO_3$, and 10.0 dextrose (295 to 305 mosmol/liter). For each brain section, one FOV in the prelimbic cortex was imaged for 900 frames in ~300 s. Images were processed with the SlideBook (Intelligent Imaging Innovations Inc.) and ImageJ software. Raw $Ca^{2+}$ imaging movies were preprocessed in ImageJ with a custom macro (GenerateHitImage.ijm, available upon request) that applied bleach correction (simple ratio, background = 100), generated a difference image between maximum-intensity and average-intensity projections, and performed rolling-ball background subtraction (radius = 20) to highlight active neurons for subsequent trace extraction and deconvolution of fluorescence signals into neural activity. Initial spatial components were defined by manually selecting candidate seed pixels from PNR graphs of the FOV (*122*). Calcium events with *z*-scores > 2 were included in analyses, and all neurons with at least one detected event were used to calculate mean $Ca^{2+}$ event rate.

### Analysis of c-$FOS^+$ cells after chemically induced seizures

Mice were administered one dose of PTZ (40 mg/kg, ip) and monitored for seizure behavior. Sixty minutes after administration of PTZ, mice that exhibited stage 7 seizures and survived were perfused with PBS followed by 4% PFA; brains were removed and post-fixed in PFA overnight. After buffer replacement with 30% sucrose, the brains were embedded and frozen in OCT compound with 7.5% sucrose. Forty-micrometer coronal brain sections were cut using a cryostat. Sections were permeabilized in PBS supplemented with 0.5% Triton X-100 and blocked for 1 hour in 10% serum. Subsequently, sections were incubated overnight at 4°C with primary antibody (rabbit anti-c-Fos; Cell Signaling Technology, #2250; 1:500), washed in PBS, and incubated at RT with Alexa Fluor–conjugated secondary antibodies for 2 hours. After incubation, sections were washed in PBS containing DAPI and mounted on Superfrost Plus slides using ProLong Gold Antifade reagent. Immunofluorescence images were collected on a Zeiss 800 confocal microscope using the ZEN Blue software. Representative tiled images were acquired at 10x. For quantification of c-$FOS^+$ cells, we collected three single *z*-plane confocal images per region per animal in L5 of the prelimbic cortex at 20x and in the dentate gyrus at 63x. Quantification of the percentage of c-$FOS^+$ cells was performed using the FIJI software by dividing by the total number of $DAPI^+$ cells. $DAPI^+$ and c-$FOS^+$ cells in the prelimbic cortex were quantified using Analyze Particles in FIJI and in the dentate gyrus by manual counting.

### Acute slice electrophysiology

Mice were anesthetized with Euthasol and perfused intracardially with 15 ml of the ice-cold cutting ACSF (described below). Brains were quickly removed and placed in the ice-cold cutting ACSF. Coronal sections (300 μm) containing the PFC were prepared in the ice-cold cutting ACSF using a vibrating blade microtome (Leica VT1200). Right after cutting, slices were recovered for 10 min at 32°C and then transferred to holding the ACSF at RT. Cutting and recovery were performed with the ACSF containing the sodium substitute NMDG (*123*): 92 mM NMDG, 20 mM Hepes (pH 7.35), 25 mM glucose, 30 mM sodium bicarbonate, 1.2 mM sodium phosphate, 2.5 mM potassium chloride, 5 mM sodium ascorbate, 3 mM sodium pyruvate, 2 mM thiourea, 10 mM magnesium, 14 mM sulfate, and 0.5 mM calcium chloride. The ACSF used for holding slices before recording was identical but contained 92 mM NaCl instead of NMDG and 1 mM $MgCl_2$ and 2 mM $CaCl_2$. The ACSF used to superfuse slices during recording contained 125 mM NaCl, 2.5 mM KCl, 1.25 mM NaH2PO4, 1 mM $MgCl_2$, 2.4 mM $CaCl_2$, 26 mM $NaHCO_3$, and 11 mM glucose. All ACSF solutions were saturated with 95% $O_2$ and 5% $CO_2$. For recording, a single slice was transferred to a heated chamber (32°C) and superfused with the normal ACSF (2.5 ml/min) using a peristaltic pump (WPI). Visualization of neurons in L5 of the PFC was achieved with an upright microscope equipped for differential interference contrast (DIC) microscopy (BX51WI, Olympus). Whole-cell patch-clamp recordings were made using a MultiClamp 700B amplifier (1-kHz low-pass Bessel filter and 10-kHz digitization) with the pClamp 10.3 software (Molecular Devices).

Voltage-clamp recordings of sEPSCs were made using glass pipets with a resistance of 2 to 4 megohms, filled with internal solution containing 117 mM cesium methanesulfonate, 20 mM Hepes, 0.4 mM EGTA, 2.8 mM NaCl, 5 mM tetraethylammonium chloride, 2.5 mM Mg-ATP, and 0.25 mM Na-GTP (pH 7.2 to 7.3 and 290 mosmol). sIPSCs were recorded with internal solution containing 136 mM CsCl, 4 mM NaCl, 1.1 mM EGTA, 10 mM Hepes, 0.2 mM $CaCl_2$, 4 mM Mg-ATP, and 0.3 mM Na-GTP (pH 7.3 and 290 mosmol). Input resistance was monitored online during recordings; cells with access resistance changes greater than 20% were excluded from analysis. Recordings were made at a −70 mV holding potential and sampled

Downloaded from https://www.science.org on August 04, 2026

at 1.8 kHz. sEPSCs were pharmacologically isolated by having gabazine (1 μM) and D,L-2-amino-5-phosphonovaleric acid (APV) (50 μM) present throughout the experiment. sIPSCs were pharmacologically isolated with 6,7-dinitroquinoxaline-2, 3-dione (DNQX; 10 μM) and APV (50 μM) in the bath. A total of 200 to 300 events per cell were analyzed, using a threshold of 2X the baseline noise. Analysis of sEPSCs and sIPSCs was performed offline using the MiniAnalysis program (v 6.0, Synaptosoft) by experimenters blind to the genotype of the animals.

Current-clamp recordings were made in the absence of drugs with internal solution containing 125 mM potassium gluconate, 0.05 mM EGTA, 10 mM Hepes, 6.27 mM KCl, 5 mM $Na_2$-phosphocreatine, 4 mM Mg-ATP, and 0.3 mM Na-GTP (pH 7.3 and 285 mosmol). Rheobase was determined by injecting 2-ms steps of positive current (increasing in 25-pA increments per sweep); values reflect the size in pA of the first current injection that elicited an action potential. The number of spikes per current clamp step was calculated from action potentials elicited by a 1-s current injection (increasing in 25-pA increments per sweep).

### Postnatal astrocyte labeling by electroporation

PALE is a medication of in utero electroporation to introduce plasmid constructs into astrocytes by shifting the age of electroporation to P0 to P1 (*124*). To perform PALE, newborn P0 pups were anesthetized by hypothermia on ice for 4 to 5 min. A plasmid mixture containing pZac2.1-GfaABC1D-Nrf2-mcherry (1 μg/μl) and pZac2.1-GfaABC1D-mCherry-*Keap1* shRNA (1 μg/μl) was injected into the lateral ventricles using a glass micropipette made from a capillary tube (Narishige, catalog no. GD-1), followed by electroporation into the ventricular zone of the cortical plate. For electroporation, electrical pulses (40 V, 50-ms duration) were delivered four times at 950-ms intervals using an electroporator (Nepagene, catalog no. CUY21EDIT).

### RNA-seq analysis of isolated astrocytes

Cortical astrocytes were acutely isolated from adult cortices by MACS cell separation. Briefly, cortical tissue samples were obtained from adult mice following saline perfusion and cortical dissection, homogenized using a papain dissociation kit (Miltenyi Biotec, #130-107-677), incubated with Fc blocking antibody and magnetic anti-ACSA-2 microbeads (Miltenyi Biotec, #130-097-679), bound to MACS LS columns (Miltenyi Biotec, #130-042-201) placed on a magnetic stand, washed three times with 0.5% BSA buffer to remove unbound cells, and eluted for downstream application. RNA was extracted from isolated astrocytes by using the PicoPure RNA isolation kit (Applied Biosystems). Samples were checked for quality/quantity on the Fragment Analyzer and Qubit before library prep [RNA quality number (RQN) > 7; 100 to 400 ng per sample]. The NEBNext Poly(A) Magnetic Isolation Module (NEB, #E7490) and NEBNext Ultra II RNA Library Prep Kit for Illumina (catalog no. E7775) were used to generate libraries. Paired-end sequencing was performed using Illumina's NovaSeq 6000 S1 200 cycle kit. Preprocessing and aligning RNA-seq reads to reference genome, differential gene expression analysis, pathway analysis, and network visualization EnrichmentMap were performed as described above (see the "RNA-seq of cortical tissue" section).

#### *Upstream TF analysis*

Through GSEA, we identified 12 GO terms related to ion channel and ion transporter activity (GO:0005216, GO:0005261, GO:0022838, GO:0015267, GO:002803, GO:0005272, GO:1905030, GO:0015672, GO:0005248, GO:0022890, GO:0006993, and GO:0055078) as biologically relevant pathways whose disturbance caused by ALDH7A1 deficiency were rescued by SFN. We next conducted CIE analysis (*59*) to identify upstream regulators of core genes (genes that contribute to the leading-edge subset within the gene set) of the GO terms related to ion channel activity identified by GSEA. Specifically, a ternary scoring statistic (*125*) was conducted to query ChIP-seq–derived TF-gene interactions from ChIP-Atlas (*126*) and identify transcriptional regulators from DEGs (relaxed cutoff of $P$ value < 0.05 was used here) identified by DESeq2.

### Statistical analysis

Representative immunofluorescence images shown were qualitatively similar across at least three animals. Individual data points are displayed for all experiments containing multiple data points. Data are reported as means ± SEM. The exact value of $n$ for each experiment is listed in the figure legends. For Western blot, ALDH7A1 cell type expression, animal weight, behavior, RNA-seq, and flow cytometry, $n$ represents the number of animals analyzed per condition. For measurements of whole-cell recordings, experiments in $cKO^{Astro(Mosaic)}$ mice, and spontaneous neuronal $Ca^{2+}$ imaging, $n$ represents the number of cells analyzed per condition, taken from at least three mice per condition. For mitochondrial stress test measurements, $n$ represents the number of primary cultures analyzed, each of which contained 10 technical replicates. For analysis of neuronal $Ca^{2+}$ imaging in response to ouabain, $n$ represents the number of acute brain slices analyzed per condition. Experimenters were blinded to group identity during experimentation and analysis (details for specific experiments described above). A specific randomization strategy was not used, and no statistical computations were performed to determine sample sizes for most experiments. We used sample sizes consistent with other studies in the field. Predefined exclusion criteria were used for pathway analysis, astrocyte acute slice calcium imaging, neuronal acute slice calcium imaging, and acute slice electrophysiology (see sections above). No other samples or data points were excluded from analysis. Statistical analyses were performed using the GraphPad Prism 10 software. Comparisons of PTZ dose-response curves were calculated by the extra sum-of-squares $F$ test of $EC_{50}$ values. $P$ values for two groups were calculated by two-tailed Student's $t$ test and between three or more groups by one-way ANOVA followed by Tukey's multiple comparison test or Dunnett's post hoc test. Comparisons between genotypes across two conditions were calculated by two-way ANOVA or mixed-model analysis followed by Holm-Sidak's multiple comparison tests between genotypes. When multiple measurements were performed in the same animal or cell, we performed a repeated-measure two-way ANOVA followed by Holm-Sidak's multiple comparison tests between genotypes. Nonparametric comparisons between three or more groups were made using the Kruskal-Wallis test with Dunn's post hoc test. Two-way nonparametric comparisons between genotypes across two conditions were made using multiple Mann-Whitney tests with Holm-Sidak correction for multiple comparisons. The statistical tests used to measure significance are indicated in each figure along with the corresponding significance level.

## Supplementary Materials

**The PDF file includes:**

Figs. S1 to S12

Legend for table S1

Downloaded from https://www.science.org on August 04, 2026

**Other Supplementary Material for this manuscript includes the following:**
Table S1

## REFERENCES


1. J. F. Tellez-Zenteno, S. B. Patten, N. Jette, J. Williams, S. Wiebe, Psychiatric comorbidity in epilepsy: A population-based analysis. *Epilepsia* **48**, 2336–2344 (2007).
2. D. C. Hesdorffer, L. Ishihara, L. Mynepalli, D. J. Webb, J. Weil, W. A. Hauser, Epilepsy, suicidality, and psychiatric disorders: A bidirectional association. *Ann. Neurol.* **72**, 184–191 (2012).
3. A. M. Kanner, Depression and epilepsy: A bidirectional relation? *Epilepsia* **52**, 21–27 (2011).
4. C. Brainstorm, V. Anttila, B. Bulik-Sullivan, H. K. Finucane, R. K. Walters, J. Bras, L. Duncan, V. Escott-Price, G. J. Falcone, P. Gormley, R. Malik, N. A. Patsopoulos, S. Ripke, Z. Wei, D. Yu, P. H. Lee, P. Turley, B. Grenier-Boley, V. Chouraki, Y. Kamatani, C. Berr, L. Letenneur, D. Hannequin, P. Amouyel, A. Boland, J. F. Deleuze, E. Duron, B. N. Vardarajan, C. Reitz, A. M. Goate, M. J. Huentelman, M. I. Kamboh, E. B. Larson, E. Rogaeva, P. St George-Hyslop, H. Hakonarson, W. A. Kukull, L. A. Farrer, L. L. Barnes, T. G. Beach, F. Y. Demirci, E. Head, C. M. Hulette, G. A. Jicha, J. S. K. Kauwe, J. A. Kaye, J. B. Leverenz, A. I. Levey, A. P. Lieberman, V. S. Pankratz, W. W. Poon, J. F. Quinn, A. J. Saykin, L. S. Schneider, A. G. Smith, J. A. Sonnen, R. A. Stern, V. M. Van Deerlin, L. J. Van Eldik, D. Harold, G. Russo, D. C. Rubinsztein, A. Bayer, M. Tsolaki, P. Proitsi, N. C. Fox, H. Hampel, M. J. Owen, S. Mead, P. Passmore, K. Morgan, M. M. Nothen, M. Rossor, M. K. Lupton, P. Hoffmann, J. Kornhuber, B. Lawlor, A. McQuillin, A. Al-Chalabi, J. C. Bis, A. Ruiz, M. Boada, S. Seshadri, A. Beiser, K. Rice, S. J. van der Lee, P. L. De Jager, D. H. Geschwind, M. Riemenschneider, S. Riedel-Heller, J. I. Rotter, G. Ransmayr, B. T. Hyman, C. Cruchaga, M. Alegret, B. Winsvold, P. Palta, K. H. Farh, E. Cuenca-Leon, N. Furlotte, T. Kurth, L. Ligthart, G. M. Terwindt, T. Freilinger, C. Ran, S. D. Gordon, G. Borck, H. H. H. Adams, T. Lehtimaki, J. Wedenoja, J. E. Buring, M. Schurks, M. Hrafnsdottir, J. J. Hottenga, B. Penninx, V. Artto, M. Kaunisto, S. Vepsalainen, N. G. Martin, G. W. Montgomery, M. I. Kurki, E. Hamalainen, H. Huang, J. Huang, C. Sandor, C. Webber, B. Muller-Myhsok, S. Schreiber, V. Salomaa, E. Loehrer, H. Gobel, A. Macaya, P. Pozo-Rosich, T. Hansen, T. Werge, J. Kaprio, A. Metspalu, C. Kubisch, M. D. Ferrari, A. C. Belin, A. van den Maagdenberg, J. A. Zwart, D. Boomsma, N. Eriksson, J. Olesen, D. I. Chasman, D. R. Nyholt, A. Avbersek, L. Baum, S. Berkovic, J. Bradfield, R. J. Buono, C. B. Catarino, P. Cossette, P. De Jonghe, C. Depondt, D. Dlugos, T. N. Ferraro, J. French, H. Hjalgrim, J. Jamnadas-Khoda, R. Kalviainen, W. S. Kunz, H. Lerche, C. Leu, D. Lindhout, W. Lo, D. Lowenstein, M. McCormack, R. S. Moller, A. Molloy, P. W. Ng, K. Oliver, M. Privitera, R. Radtke, A. K. Ruppert, T. Sander, S. Schachter, C. Schankin, I. Scheffer, S. Schoch, S. M. Sisodiya, P. Smith, M. Sperling, P. Striano, R. Surges, G. N. Thomas, F. Visscher, C. D. Whelan, F. Zara, E. L. Heinzen, A. Marson, F. Becker, H. Stroink, F. Zimprich, T. Gasser, R. Gibbs, P. Heutink, M. Martinez, H. R. Morris, M. Sharma, M. Ryten, K. Y. Mok, S. Pulit, S. Bevan, E. Holliday, J. Attia, T. Battey, G. Boncoraglio, V. Thijs, W. M. Chen, B. Mitchell, P. Rothwell, P. Sharma, C. Sudlow, A. Vicente, H. Markus, C. Kourkoulis, J. Pera, M. Raffeld, S. Silliman, V. Boraska Perica, L. M. Thornton, L. M. Huckins, N. William Rayner, C. M. Lewis, M. Gratacos, F. Rybakowski, A. Keski-Rahkonen, A. Raevuori, J. I. Hudson, T. Reichborn-Kjennerud, P. Monteleone, A. Karwautz, K. Mannik, J. H. Baker, J. K. O'Toole, S. E. Trace, O. S. P. Davis, S. G. Helder, S. Ehrlich, B. Herpertz-Dahlmann, U. N. Danner, A. A. van Elburg, M. Clementi, M. Forzan, E. Docampo, J. Lissowska, J. Hauser, A. Tortorella, M. Maj, F. Gonidakis, K. Tziouvas, H. Papezova, Z. Yilmaz, G. Wagner, S. Cohen-Woods, S. Herms, A. Julia, R. Rabionet, D. M. Dick, S. Ripatti, O. A. Andreassen, T. Espeseth, A. J. Lundervold, V. M. Steen, D. Pinto, S. W. Scherer, H. Aschauer, A. Schosser, L. Alfredsson, L. Padyukov, K. A. Halmi, J. Mitchell, M. Strober, A. W. Bergen, W. Kaye, J. P. Szatkiewicz, B. Cormand, J. A. Ramos-Quiroga, C. Sanchez-Mora, M. Ribases, M. Casas, A. Hervas, M. J. Arranz, J. Haavik, T. Zayats, S. Johansson, N. Williams, A. Dempfle, A. Rothenberger, J. Kuntsi, R. D. Oades, T. Banaschewski, B. Franke, J. K. Buitelaar, A. Arias Vasquez, A. E. Doyle, A. Reif, K. P. Lesch, C. Freitag, O. Rivero, H. Palmason, M. Romanos, K. Langley, M. Rietschel, S. H. Witt, S. Dalsgaard, A. D. Borglum, I. Waldman, B. Wilmot, N. Molly, C. H. D. Bau, J. Crosbie, R. Schachar, S. K. Loo, J. J. McGough, E. H. Grevet, S. E. Medland, E. Robinson, L. A. Weiss, E. Bacchelli, A. Bailey, V. Bal, A. Battaglia, C. Betancur, P. Bolton, R. Cantor, P. Celestino-Soper, G. Dawson, S. De Rubeis, F. Duque, A. Green, S. M. Klauck, M. Leboyer, P. Levitt, E. Maestrini, S. Mane, D. M. De-Luca, J. Parr, R. Regan, A. Reichenberg, S. Sandin, J. Vorstman, T. Wassink, E. Wijsman, E. Cook, S. Santangelo, R. Delorme, B. Roge, T. Magalhaes, D. Arking, T. G. Schulze, R. C. Thompson, J. Strohmaier, K. Matthews, I. Melle, D. Morris, D. Blackwood, A. McIntosh, S. E. Bergen, M. Schalling, S. Jamain, A. Maaser, S. B. Fischer, C. S. Reinbold, J. M. Fullerton, J. Guzman-Parra, F. Mayoral, P. R. Schofield, S. Cichon, T. W. Muhleisen, F. Degenhardt, J. Schumacher, M. Bauer, P. B. Mitchell, E. S. Gershon, J. Rice, J. B. Potash, P. P. Zandi, N. Craddock, I. N. Ferrier, M. Alda, G. A. Rouleau, G. Turecki, R. Ophoff, C. Pato, A. Anjorin, E. Stahl, M. Leber, P. M. Czerski, C. Cruceanu, I. R. Jones, D. Posthuma, T. F. M. Andlauer, A. J. Forstner, F. Streit, B. T. Baune, T. Air, G. Sinnamon, N. R. Wray, D. J. MacIntyre, D. Porteous, G. Homuth, M. Rivera, J. Grove, C. M. Middeldorp, I. Hickie, M. Pergadia, D. Mehta, J. H. Smit, R. Jansen, E. de Geus, E. Dunn, Q. S. Li, M. Nauck, R. A. Schoevers, A. T. Beekman, J. A. Knowles, A. Viktorin, P. Arnold, C. L. Barr, G. Bedoya-Berrio, O. J. Bienvenu, H. Brentani, C. Burton, B. Camarena, C. Cappi, D. Cath, M. Cavallini, D. Cusi, S. Darrow, D. Denys, E. M. Derks, A. Dietrich, T. Fernandez, M. Figee, N. Freimer, G. Gerber, M. Grados, E. Greenberg, G. L. Hanna, A. Hartmann, M. E. Hirschtritt, P. J. Hoekstra, A. Huang, C. Huyser, C. Illmann, M. Jenike, S. Kuperman, B. Leventhal, C. Lochner, G. J. Lyon, F. Macciardi, M. Madruga-Garrido, I. A. Malaty, A. Maras, L. McGrath, E. C. Miguel, P. Mir, G. Nestadt, H. Nicolini, M. S. Okun, A. Pakstis, P. Paschou, J. Piacentini, C. Pittenger, K. Plessen, V. Ramensky, E. M. Ramos, V. Reus, M. A. Richter, M. A. Riddle, M. M. Robertson, V. Roessner, M. Rosario, J. F. Samuels, P. Sandor, D. J. Stein, F. Tsetsos, F. Van Nieuwerburgh, S. Weatherall, J. R. Wendland, T. Wolanczyk, Y. Worbe, G. Zai, F. S. Goes, N. McLaughlin, P. S. Nestadt, H. J. Grabe, C. Depienne, A. Konkashbaev, N. Lanzagorta, A. Valencia-Duarte, E. Bramon, N. Buccola, W. Cahn, M. Cairns, S. A. Chong, D. Cohen, B. Crespo-Facorro, J. Crowley, M. Davidson, L. DeLisi, T. Dinan, G. Donohoe, E. Drapeau, J. Duan, L. Haan, D. Hougaard, S. Karachanak-Yankova, A. Khrunin, J. Klovins, V. Kucinskas, J. L. C. Keong, S. Limborska, C. Loughland, J. Lonnqvist, B. Maher, M. Mattheisen, C. McDonald, K. C. Murphy, I. Nenadic, J. van Os, C. Pantelis, M. Pato, T. Petryshen, D. Quested, P. Roussos, A. R. Sanders, U. Schall, S. G. Schwab, K. Sim, H. C. So, E. Stogmann, M. Subramaniam, D. Toncheva, J. Waddington, J. Walters, M. Weiser, W. Cheng, R. Cloninger, D. Curtis, P. V. Gejman, F. Henskens, M. Mattingsdal, S. Y. Oh, R. Scott, B. Webb, G. Breen, C. Churchhouse, C. M. Bulik, M. Daly, M. Dichgans, S. V. Faraone, R. Guerreiro, P. Holmans, K. S. Kendler, B. Koeleman, C. A. Mathews, A. Price, J. Scharf, P. Sklar, J. Williams, N. W. Wood, C. Cotsapas, A. Palotie, J. W. Smoller, P. Sullivan, J. Rosand, A. Corvin, B. M. Neale, J. M. Schott, R. Anney, J. Elia, M. Grigoroiu-Serbanescu, H. J. Edenberg, R. Murray, Analysis of shared heritability in common disorders of the brain. *Science* **360**, eaap8757 (2018).
5. N. G. Cascella, D. J. Schretlen, A. Sawa, Schizophrenia and epilepsy: Is there a shared susceptibility? *Neurosci. Res.* **63**, 227–235 (2009).
6. B. J. Insel, R. Ottman, G. A. Heiman, Mood disorders in familial epilepsy: A test of shared etiology. *Epilepsia* **59**, 431–439 (2018).
7. S. E. Antonarakis, J. S. Beckmann, Mendelian disorders deserve more attention. *Nat. Rev. Genet.* **7**, 277–282 (2006).
8. P. B. Mills, E. Struys, C. Jakobs, B. Plecko, P. Baxter, M. Baumgartner, M. A. Willemsen, H. Omran, U. Tacke, B. Uhlenberg, B. Weschke, P. T. Clayton, Mutations in antiquitin in individuals with pyridoxine-dependent seizures. *Nat. Med.* **12**, 307–309 (2006).
9. P. Baxter, P. Griffiths, T. Kelly, D. Gardner-Medwin, Pyridoxine-dependent seizures: Demographic, clinical, MRI and psychometric features, and effect of dose on intelligence quotient. *Dev. Med. Child Neurol.* **38**, 998–1006 (1996).
10. K. Baynes, S. T. Farias, S. M. Gospe Jr., Pyridoxine-dependent seizures and cognition in adulthood. *Dev. Med. Child Neurol.* **45**, 782–785 (2003).
11. Y. Zhang, S. A. Sloan, L. E. Clarke, C. Caneda, C. A. Plaza, P. D. Blumenthal, H. Vogel, G. K. Steinberg, M. S. Edwards, G. Li, J. A. Duncan III, S. H. Cheshier, L. M. Shuer, E. F. Chang, G. A. Grant, M. G. Gephart, B. A. Barres, Purification and characterization of progenitor and mature human astrocytes reveals transcriptional and functional differences with mouse. *Neuron* **89**, 37–53 (2016).
12. A. Verkhratsky, M. Nedergaard, L. Hertz, Why are astrocytes important? *Neurochem. Res.* **40**, 389–401 (2015).
13. N. J. Allen, C. Eroglu, Cell biology of astrocyte-synapse interactions. *Neuron* **96**, 697–708 (2017).
14. U. Pannasch, L. Vargova, J. Reingruber, P. Ezan, D. Holcman, C. Giaume, E. Sykova, N. Rouach, Astroglial networks scale synaptic activity and plasticity. *Proc. Natl. Acad. Sci. U.S.A.* **108**, 8467–8472 (2011).
15. V. Vasiliou, D. W. Nebert, Analysis and update of the human aldehyde dehydrogenase (ALDH) gene family. *Hum. Genomics* **2**, 138–143 (2005).
16. M. F. Wang, C. L. Han, S. J. Yin, Substrate specificity of human and yeast aldehyde dehydrogenases. *Chem. Biol. Interact.* **178**, 36–39 (2009).
17. T. D. Missihoun, S. O. Kotchoni, D. Bartels, Aldehyde dehydrogenases function in the homeostasis of pyridine nucleotides in Arabidopsis thaliana. *Sci. Rep.* **8**, 2936 (2018).
18. S. Singh, C. Brocker, V. Koppaka, Y. Chen, B. C. Jackson, A. Matsumoto, D. C. Thompson, V. Vasiliou, Aldehyde dehydrogenases in cellular responses to oxidative/electrophilic stress. *Free Radic. Biol. Med.* **56**, 89–101 (2013).
19. J. S. Yang, J. W. Hsu, S. Y. Park, S. Y. Lee, J. Li, M. Bai, C. Alves, W. Tseng, X. Michelet, I. C. Ho, V. W. Hsu, ALDH7A1 inhibits the intracellular transport pathways during hypoxia and starvation to promote cellular energy homeostasis. *Nat. Commun.* **10**, 4068 (2019).
20. J. S. Yang, A. J. Morris, K. Kamizaki, J. Chen, J. Stark, W. M. Oldham, T. Nakamura, E. Mishima, J. Loscalzo, Y. Minami, M. Conrad, W. S. Henry, V. W. Hsu, ALDH7A1 protects against ferroptosis by generating membrane NADH and regulating FSP1. *Cell* **188**, 2569–2585.e20 (2025).
21. P. J. O'Brien, A. G. Siraki, N. Shangari, Aldehyde sources, metabolism, molecular toxicity mechanisms, and possible effects on human health. *Crit. Rev. Toxicol.* **35**, 609–662 (2005).
22. V. Vasiliou, A. Pappa, T. Estey, Role of human aldehyde dehydrogenases in endobiotic and xenobiotic metabolism. *Drug Metab. Rev.* **36**, 279–299 (2004).


Downloaded from https://www.science.org on August 04, 2026

23. R. M. LoPachin, T. Gavin, Molecular mechanisms of aldehyde toxicity: A chemical perspective. *Chem. Res. Toxicol.* **27**, 1081–1091 (2014).
24. D. W. Nebert, A. L. Roe, M. Z. Dieter, W. A. Solis, Y. Yang, T. P. Dalton, Role of the aromatic hydrocarbon receptor and [Ah] gene battery in the oxidative stress response, cell cycle control, and apoptosis. *Biochem. Pharmacol.* **59**, 65–85 (2000).
25. L. Uma, J. Hariharan, Y. Sharma, D. Balasubramanian, Corneal aldehyde dehydrogenase displays antioxidant properties. *Exp. Eye Res.* **63**, 117–119 (1996).
26. M. Erecinska, I. A. Silver, Tissue oxygen tension and brain sensitivity to hypoxia. *Respir. Physiol.* **128**, 263–276 (2001).
27. H. H. Al-Shekaili, T. L. Petkau, I. Pena, T. C. Lengyell, N. M. Verhoeven-Duif, J. Ciapaite, M. Bosma, M. van Faassen, I. P. Kema, G. Horvath, C. Ross, E. M. Simpson, J. M. Friedman, C. van Karnebeek, B. R. Leavitt, A novel mouse model for pyridoxine-dependent epilepsy due to antiquitin deficiency. *Hum. Mol. Genet.* **29**, 3266–3284 (2020).
28. I. A. Pena, Y. Roussel, K. Daniel, K. Mongeon, D. Johnstone, H. Weinschutz Mendes, M. Bosma, V. Saxena, N. Lepage, P. Chakraborty, D. A. Dyment, C. D. M. van Karnebeek, N. Verhoeven-Duif, T. V. Bui, K. M. Boycott, M. Ekker, A. MacKenzie, Pyridoxine-dependent epilepsy in zebrafish caused by Aldh7a1 deficiency. *Genetics* **207**, 1501–1518 (2017).
29. N. Zabinyakov, G. Bullivant, F. Cao, M. Fernandez Ojeda, Z. P. Jia, X. Y. Wen, J. J. Dowling, G. S. Salomons, S. Mercimek-Andrews, Characterization of the first knock-out aldh7a1 zebrafish model for pyridoxine-dependent epilepsy using CRISPR-Cas9 technology. *PLOS ONE* **12**, e0186645 (2017).
30. J. Yan, J. Wu, M. Xu, M. Wang, W. Guo, Disrupted de novo pyrimidine biosynthesis impairs adult hippocampal neurogenesis and cognition in pyridoxine-dependent epilepsy. *Sci. Adv.* **10**, eadl2764 (2024).
31. R. Kobau, F. Gilliam, D. J. Thurman, Prevalence of self-reported epilepsy or seizure disorder and its associations with self-reported depression and anxiety: Results from the 2004 HealthStyles Survey. *Epilepsia* **47**, 1915–1921 (2006).
32. C. D. van Karnebeek, S. A. Tiebout, J. Niermeijer, B. T. Poll-The, A. Ghani, C. R. Coughlin II, J. L. Van Hove, J. W. Richter, H. J. Christen, R. Gallagher, H. Hartmann, S. Stockler-Ipsiroglu, Pyridoxine-dependent epilepsy: An expanding clinical spectrum. *Pediatr. Neurol.* **59**, 6–12 (2016).
33. E. Beurel, M. Toups, C. B. Nemeroff, The bidirectional relationship of depression and inflammation: Double trouble. *Neuron* **107**, 234–256 (2020).
34. M. Vavakova, Z. Durackova, J. Trebaticka, Markers of oxidative stress and neuroprogression in depression disorder. *Oxid. Med. Cell. Longev.* **2015**, 898393 (2015).
35. R. S. Duman, G. Sanacora, J. H. Krystal, Altered connectivity in depression: GABA and glutamate neurotransmitter deficits and reversal by novel treatments. *Neuron* **102**, 75–90 (2019).
36. Q. Wang, W. Jie, J. H. Liu, J. M. Yang, T. M. Gao, An astroglial basis of major depressive disorder? An overview. *Glia* **65**, 1227–1250 (2017).
37. D. A. Slattery, J. F. Cryan, Using the rat forced swim test to assess antidepressant-like activity in rodents. *Nat. Protoc.* **7**, 1009–1014 (2012).
38. G. Chevalier, E. Siopi, L. Guenin-Mace, M. Pascal, T. Laval, A. Rifflet, I. G. Boneca, C. Demangel, B. Colsch, A. Pruvost, E. Chu-Van, A. Messager, F. Leulier, G. Lepousez, G. Eberl, P. M. Lledo, Effect of gut microbiota on depressive-like behaviors in mice is mediated by the endocannabinoid system. *Nat. Commun.* **11**, 6363 (2020).
39. J. F. Cryan, R. J. Valentino, I. Lucki, Assessing substrates underlying the behavioral effects of antidepressants using the modified rat forced swimming test. *Neurosci. Biobehav. Rev.* **29**, 547–569 (2005).
40. J. F. Rodriguez-Landa, C. M. Contreras, B. Bernal-Morales, A. G. Gutierrez-Garcia, M. Saavedra, Allopregnanolone reduces immobility in the forced swimming test and increases the firing rate of lateral septal neurons through actions on the $GABA_A$ receptor in the rat. *J. Psychopharmacol.* **21**, 76–84 (2007).
41. P. Zanos, R. Moaddel, P. J. Morris, P. Georgiou, J. Fischell, G. I. Elmer, M. Alkondon, P. Yuan, H. J. Pribut, N. S. Singh, K. S. Dossou, Y. Fang, X. P. Huang, C. L. Mayo, I. W. Wainer, E. X. Albuquerque, S. M. Thompson, C. J. Thomas, C. A. Zarate Jr., T. D. Gould, NMDAR inhibition-independent antidepressant actions of ketamine metabolites. *Nature* **533**, 481–486 (2016).
42. M. R. Warden, A. Selimbeyoglu, J. J. Mirzabekov, M. Lo, K. R. Thompson, S. Y. Kim, A. Adhikari, K. M. Tye, L. M. Frank, K. Deisseroth, A prefrontal cortex-brainstem neuronal projection that controls response to behavioural challenge. *Nature* **492**, 428–432 (2012).
43. J. A. Gorski, T. Talley, M. Qiu, L. Puelles, J. L. Rubenstein, K. R. Jones, Cortical excitatory neurons and glia, but not GABAergic neurons, are produced in the Emx1-expressing lineage. *J. Neurosci.* **22**, 6309–6314 (2002).
44. C. Brocker, N. Lassen, T. Estey, A. Pappa, M. Cantore, V. V. Orlova, T. Chavakis, K. L. Kavanagh, U. Oppermann, V. Vasiliou, Aldehyde dehydrogenase 7A1 (ALDH7A1) is a novel enzyme involved in cellular defense against hyperosmotic stress. *J. Biol. Chem.* **285**, 18452–18463 (2010).
45. J. Reimand, R. Isserlin, V. Voisin, M. Kucera, C. Tannus-Lopes, A. Rostamianfar, L. Wadi, M. Meyer, J. Wong, C. Xu, D. Merico, G. D. Bader, Pathway enrichment analysis and visualization of omics data using g:Profiler, GSEA, Cytoscape and EnrichmentMap. *Nat. Protoc.* **14**, 482–517 (2019).
46. S. Stockler, B. Plecko, S. M. Gospe Jr., M. Coulter-Mackie, M. Connolly, C. van Karnebeek, S. Mercimek-Mahmutoglu, H. Hartmann, G. Scharer, E. Struijs, I. Tein, C. Jakobs, P. Clayton, J. L. Van Hove, Pyridoxine dependent epilepsy and antiquitin deficiency: Clinical and molecular characteristics and recommendations for diagnosis, treatment and follow-up. *Mol. Genet. Metab.* **104**, 48–60 (2011).
47. M. Gutscher, A. L. Pauleau, L. Marty, T. Brach, G. H. Wabnitz, Y. Samstag, A. J. Meyer, T. P. Dick, Real-time imaging of the intracellular glutathione redox potential. *Nat. Methods* **5**, 553–559 (2008).
48. B. C. Cox, Z. Liu, M. M. Lagarde, J. Zuo, Conditional gene expression in the mouse inner ear using Cre-loxP. *J. Assoc. Res. Otolaryngol.* **13**, 295–322 (2012).
49. A. Agarwal, P. H. Wu, E. G. Hughes, M. Fukaya, M. A. Tischfield, A. J. Langseth, D. Wirtz, D. E. Bergles, Transient opening of the mitochondrial permeability transition pore induces microdomain calcium transients in astrocyte processes. *Neuron* **93**, 587–605.e7 (2017).
50. A. L. Nieminen, A. M. Byrne, B. Herman, J. J. Lemasters, Mitochondrial permeability transition in hepatocytes induced by t-BuOOH: NAD(P)H and reactive oxygen species. *Am. J. Physiol.* **272**, C1286–C1294 (1997).
51. S. Joko, M. Watanabe, H. Fuda, S. Takeda, T. Furukawa, S.-P. Hui, R. Shrestha, H. Chiba, Hitoshi Chiba, Comparison of chemical structures and cytoprotection abilities between direct and indirect antioxidants. *J. Funct. Foods* **35**, 245–255 (2017).
52. L. F. Cardozo, L. M. Pedruzzi, P. Stenvinkel, M. B. Stockler-Pinto, J. B. Daleprane, M. Leite Jr., D. Mafra, Nutritional strategies to modulate inflammation and oxidative stress pathways via activation of the master antioxidant switch Nrf2. *Biochimie* **95**, 1525–1533 (2013).
53. A. Kobayashi, M. I. Kang, H. Okawa, M. Ohtsuji, Y. Zenke, T. Chiba, K. Igarashi, M. Yamamoto, Oxidative stress sensor Keap1 functions as an adaptor for Cul3-based E3 ligase to regulate proteasomal degradation of Nrf2. *Mol. Cell. Biol.* **24**, 7130–7139 (2004).
54. T. W. Kensler, P. A. Egner, A. S. Agyeman, K. Visvanathan, J. D. Groopman, J. G. Chen, T. Y. Chen, J. W. Fahey, P. Talalay, Keap1-nrf2 signaling: A target for cancer prevention by sulforaphane. *Top. Curr. Chem.* **329**, 163–177 (2013).
55. A. Bellot-Saez, O. Kekesi, J. W. Morley, Y. Buskila, Astrocytic modulation of neuronal excitability through $K^+$ spatial buffering. *Neurosci. Biobehav. Rev.* **77**, 87–97 (2017).
56. A. Verkhratsky, M. Nedergaard, Physiology of astroglia. *Physiol. Rev.* **98**, 239–389 (2018).
57. L. Hertz, D. Song, J. Xu, L. Peng, M. E. Gibbs, Role of the astrocytic $Na^+$, $K^+$-ATPase in $K^+$ homeostasis in brain: $K^+$ Uptake, signaling pathways and substrate utilization. *Neurochem. Res.* **40**, 2505–2516 (2015).
58. E. M. Hwang, E. Kim, O. Yarishkin, D. H. Woo, K. S. Han, N. Park, Y. Bae, J. Woo, D. Kim, M. Park, C. J. Lee, J. Y. Park, A disulphide-linked heterodimer of TWIK-1 and TREK-1 mediates passive conductance in astrocytes. *Nat. Commun.* **5**, 3227 (2014).
59. S. Farahmand, C. O'Connor, J. A. Macoska, K. Zarringhalam, Causal Inference Engine: A platform for directional gene set enrichment analysis and inference of active transcriptional regulators. *Nucleic Acids Res.* **47**, 11563–11573 (2019).
60. Q. Li, Z. W. Zhou, W. Duan, C. Y. Qian, S. N. Wang, M. S. Deng, D. Zi, J. M. Wang, C. Y. Mao, G. Song, D. Wang, K. D. Westover, C. X. Xu, Inhibiting the redox function of APE1 suppresses cervical cancer metastasis via disengagement of ZEB1 from E-cadherin in EMT. *J. Exp. Clin. Cancer Res.* **40**, 220 (2021).
61. Y. Guan, E. F. Greenberg, M. Hasipek, S. Chen, X. Liu, C. M. Kerr, D. Gackowski, E. Zarakowska, T. Radivoyevitch, X. Gu, B. Willard, V. Visconte, H. Makishima, A. Nazha, M. Mukherji, M. A. Sekeres, Y. Saunthararajah, R. Olinski, M. Xu, J. P. Maciejewski, B. K. Jha, Context dependent effects of ascorbic acid treatment in TET2 mutant myeloid neoplasia. *Commun. Biol.* **3**, 493 (2020).
62. R. M. Liu, L. P. Desai, Reciprocal regulation of TGF-β and reactive oxygen species: A perverse cycle for fibrosis. *Redox Biol.* **6**, 565–577 (2015).
63. X. Qu, L. Yan, R. Guo, H. Li, Z. Shi, ROS-induced GATA4 and GATA6 downregulation inhibits StAR expression in LPS-treated porcine granulosa-lutein cells. *Oxid. Med. Cell. Longev.* **2019**, 5432792 (2019).
64. E. J. Uhlmann, M. Wong, R. L. Baldwin, M. L. Bajenaru, H. Onda, D. J. Kwiatkowski, K. Yamada, D. H. Gutmann, Astrocyte-specific TSC1 conditional knockout mice exhibit abnormal neuronal organization and seizures. *Ann. Neurol.* **52**, 285–296 (2002).
65. H. Higashimori, C. S. Schin, M. S. Chiang, L. Morel, T. A. Shoneye, D. L. Nelson, Y. Yang, Selective deletion of astroglial FMRP dysregulates glutamate transporter GLT1 and contributes to fragile X syndrome phenotypes in vivo. *J. Neurosci.* **36**, 7079–7094 (2016).
66. D. T. Lioy, S. K. Garg, C. E. Monaghan, J. Raber, K. D. Foust, B. K. Kaspar, P. G. Hirrlinger, F. Kirchhoff, J. M. Bissonnette, N. Ballas, G. Mandel, A role for glia in the progression of Rett's syndrome. *Nature* **475**, 497–500 (2011).
67. Tabula Muris Consortium, Overall coordination, Logistical coordination, Organ collection and processing, Library preparation and sequencing, Computational data analysis, Cell type annotation, Writing group, Supplemental text writing group, Principal investigators, Single-cell transcriptomics of 20 mouse organs creates a Tabula Muris. *Nature* **562**, 367–372 (2018).
68. Tabula Sapiens Consortium, R. C. Jones, J. Karkanias, M. A. Krasnow, A. O. Pisco, S. R. Quake, J. Salzman, N. Yosef, B. Bulthaup, P. Brown, W. Harper, M. Hemenez, R. Ponnusamy, A. Salehi, B. A. Sanagavarapu, E. Spallino, K. A. Aaron, W. Concepcion,


Downloaded from https://www.science.org on August 04, 2026

J. M. Gardner, B. Kelly, N. Neidlinger, Z. Wang, S. Crasta, S. Kolluru, M. Morri, S. Y. Tan, K. J. Travaglini, C. Xu, M. Alcantara-Hernandez, N. Almanzar, J. Antony, B. Beyersdorf, D. Burhan, K. Calcuttawala, M. M. Carter, C. K. F. Chan, C. A. Chang, S. Chang, A. Colville, R. N. Culver, I. Cvijovic, G. D'Amato, C. Ezran, F. X. Galdos, A. Gillich, W. R. Goodyer, Y. Hang, A. Hayashi, S. Houshdaran, X. Huang, J. C. Irwin, S. Jang, J. V. Juanico, A. M. Kershner, S. Kim, B. Kiss, W. Kong, M. E. Kumar, A. H. Kuo, B. Li, G. B. Loeb, W. J. Lu, S. Mantri, M. Markovic, P. L. McAlpine, A. de Morree, K. Mrouj, S. Mukherjee, T. Muser, P. Neuhofer, T. D. Nguyen, K. Perez, N. Puluca, Z. Qi, P. Rao, H. Raquer-McKay, N. Schaum, B. Scott, B. Seddighzadeh, J. Segal, S. Sen, S. Sikandar, S. P. Spencer, L. C. Steffes, V. R. Subramaniam, A. Swarup, M. Swift, W. Van Treuren, E. Trimm, S. Veizades, S. Vijayakumar, K. C. Vo, S. K. Vorperian, W. Wang, H. N. W. Weinstein, J. Winkler, T. T. H. Wu, J. Xie, A. R. Yung, Y. Zhang, A. M. Detweiler, H. Mekonen, N. F. Neff, R. V. Sit, M. Tan, J. Yan, G. R. Bean, V. Charu, E. Forgo, B. A. Martin, M. G. Ozawa, O. Silva, A. Toland, V. N. P. Vemuri, S. Afik, K. Awayan, O. B. Botvinnik, A. Byrne, M. Chen, R. Dehghannasiri, A. Gayoso, A. A. Granados, Q. Li, G. Mahmoudabadi, A. McGeever, J. E. Olivieri, M. Park, N. Ravikumar, G. Stanley, W. Tan, A. J. Tarashansky, R. Vanheusden, P. Wang, S. Wang, G. Xing, L. Dethlefsen, C. Ezran, A. Gillich, Y. Hang, P. Y. Ho, J. C. Irwin, S. Jang, R. Leylek, S. Liu, J. S. Maltzman, R. J. Metzger, R. Phansalkar, K. Sasagawa, R. Sinha, H. Song, A. Swarup, E. Trimm, S. Veizades, B. Wang, P. A. Beachy, M. F. Clarke, L. C. Giudice, F. W. Huang, K. C. Huang, J. Idoyaga, S. K. Kim, C. S. Kuo, P. Nguyen, T. A. Rando, K. Red-Horse, J. Reiter, D. A. Relman, J. L. Sonnenburg, A. Wu, S. M. Wu, T. Wyss-Coray, The Tabula Sapiens: A multiple-organ, single-cell transcriptomic atlas of humans. *Science* **376**, eabl4896 (2022).

69. C. F. Rose, P. Amodio, J. S. Bajaj, R. K. Dhiman, S. Montagnese, S. D. Taylor-Robinson, H. Vilstrup, R. Jalan, Hepatic encephalopathy: Novel insights into classification, pathophysiology and therapy. *J. Hepatol.* **73**, 1526–1547 (2020).
70. D. M. Ficker, B. F. Westmoreland, F. W. Sharbrough, Epileptiform abnormalities in hepatic encephalopathy. *J. Clin. Neurophysiol.* **14**, 230–234 (1997).
71. A. U. Amaral, M. Wajner, Pathophysiology of maple syrup urine disease: Focus on the neurotoxic role of the accumulated branched-chain amino acids and branched-chain α-keto acids. *Neurochem. Int.* **157**, 105360 (2022).
72. J. Kido, K. Nakamura, Hyperammonemia in urea cycle disorders: A toxic metabolite for the brain. *Pediatr. Int.* **67**, e70121 (2025).
73. H. Blumenfeld, Cellular and network mechanisms of spike-wave seizures. *Epilepsia* **46**, 21–33 (2005).
74. J. Gotman, C. Grova, A. Bagshaw, E. Kobayashi, Y. Aghakhani, F. Dubeau, Generalized epileptic discharges show thalamocortical activation and suspension of the default state of the brain. *Proc. Natl. Acad. Sci. U.S.A.* **102**, 15236–15240 (2005).
75. H. Jokeit, R. J. Seitz, H. J. Markowitsch, N. Neumann, O. W. Witte, A. Ebner, Prefrontal asymmetric interictal glucose hypometabolism and cognitive impairment in patients with temporal lobe epilepsy. *Brain* **120**, 2283–2294 (1997).
76. M. Song, H. Du, N. Wu, B. Hou, G. Wu, J. Wang, H. Feng, T. Jiang, Impaired resting-state functional integrations within default mode network of generalized tonic-clonic seizures epilepsy. *PLOS ONE* **6**, e17294 (2011).
77. W. Walz, Role of astrocytes in the clearance of excess extracellular potassium. *Neurochem. Int.* **36**, 291–300 (2000).
78. P. Kofuji, E. A. Newman, Potassium buffering in the central nervous system. *Neuroscience* **129**, 1045–1056 (2004).
79. D. Lichtstein, A. Ilani, H. Rosen, N. Horesh, S. V. Singh, N. Buzaglo, A. Hodes, $Na^+$, $K^+$-ATPase signaling and bipolar disorder. *Int. J. Mol. Sci.* **19**, 2314 (2018).
80. S. Della Vecchia, M. Marchese, F. M. Santorelli, F. Sicca, Kir4.1 dysfunction in the pathophysiology of depression: A systematic review. *Cells* **10**, 2628 (2021).
81. Z. Xiong, K. Zhang, Q. Ren, L. Chang, J. Chen, K. Hashimoto, Increased expression of inwardly rectifying Kir4.1 channel in the parietal cortex from patients with major depressive disorder. *J. Affect. Disord.* **245**, 265–269 (2019).
82. Y. Cui, Y. Yang, Z. Ni, Y. Dong, G. Cai, A. Foncelle, S. Ma, K. Sang, S. Tang, Y. Li, Y. Shen, H. Berry, S. Wu, H. Hu, Astroglial Kir4.1 in the lateral habenula drives neuronal bursts in depression. *Nature* **554**, 323–327 (2018).
83. L. Li, H. Wu, J. Qian, M. Li, Y. Li, B. Li, Y. Han, Y. Du, Y. Wang, K. Matand, N. Wu, Decreased Na+/K+ ATPase α1 (ATP1A1) gene expression in major depression patients' peripheral blood. *Cent. Eur. J. Biol.* **8**, 1077–1082 (2013).
84. I. Goldstein, E. Lerer, E. Laiba, J. Mallet, M. Mujaheed, C. Laurent, H. Rosen, R. P. Ebstein, D. Lichtstein, Association between sodium- and potassium-activated adenosine triphosphatase α isoforms and bipolar disorders. *Biol. Psychiatry* **65**, 985–991 (2009).
85. G. S. Kirshenbaum, K. Saltzman, B. Rose, J. Petersen, B. Vilsen, J. C. Roder, Decreased neuronal Na+, K+ -ATPase activity in Atp1a3 heterozygous mice increases susceptibility to depression-like endophenotypes by chronic variable stress. *Genes Brain Behav.* **10**, 542–550 (2011).
86. H. Song, S. M. Thompson, M. P. Blaustein, Nanomolar ouabain augments $Ca2^+$ signalling in rat hippocampal neurones and glia. *J. Physiol.* **591**, 1671–1689 (2013).
87. M. Duque, A. B. Chen, E. Hsu, S. Narayan, A. Rymbek, S. Begum, G. Saher, A. E. Cohen, D. E. Olson, Y. Li, D. A. Prober, D. E. Bergles, M. C. Fishman, F. Engert, M. B. Ahrens, Ketamine induces plasticity in a norepinephrine-astroglial circuit to promote behavioral perseverance. *Neuron* **113**, 426–443.e5 (2025).
88. C. Murphy-Royal, A. D. Johnston, A. K. J. Boyce, B. Diaz-Castro, A. Institoris, G. Peringod, O. Zhang, R. F. Stout, D. C. Spray, R. J. Thompson, B. S. Khakh, J. S. Bains, G. R. Gordon, Stress gates an astrocytic energy reservoir to impair synaptic plasticity. *Nat. Commun.* **11**, 2014 (2020).
89. Y. Bansal, S. A. Codeluppi, M. Banasr, Astroglial dysfunctions in mood disorders and rodent stress Models: Consequences on behavior and potential as treatment target. *Int. J. Mol. Sci.* **25**, 6357 (2024).
90. J. Wu, D. Qin, Z. Liang, Q. Liu, M. Wang, Y. Guo, W. Guo, Dysregulation of astrocyte-derived matrix gla protein impairs dendritic spine development in pyridoxine-dependent epilepsy. *Mol. Ther.* **33**, 1785–1802 (2025).
91. C. R. Coughlin II, L. A. Tseng, J. E. Abdenur, C. Ashmore, F. Boemer, L. A. Bok, M. Boyer, D. Buhas, P. T. Clayton, A. Das, H. Dekker, A. Evangeliou, F. Feillet, E. J. Footitt, S. M. Gospe Jr., H. Hartmann, M. Kara, E. Kristensen, J. Lee, R. Lilje, N. Longo, R. J. Lunsing, P. Mills, M. T. Papadopoulou, P. L. Pearl, F. Piazzon, B. Plecko, A. G. Saini, S. Santra, D. R. Sjarif, S. Stockler-Ipsiroglu, P. Striano, J. L. K. Van Hove, N. M. Verhoeven-Duif, F. A. Wijburg, S. M. Zuberi, C. D. M. van Karnebeek, Consensus guidelines for the diagnosis and management of pyridoxine-dependent epilepsy due to α-aminoadipic semialdehyde dehydrogenase deficiency. *J. Inherit. Metab. Dis.* **44**, 178–192 (2021).
92. F. Ghazizadeh-Hashemi, S. Bagheri, A. Ashraf-Ganjouei, K. Moradi, N. Shahmansouri, M. Mehrpooya, A. A. Noorbala, S. Akhondzadeh, Efficacy and safety of sulforaphane for treatment of mild to moderate depression in patients with history of cardiac interventions: A randomized, double-blind, placebo-controlled clinical trial. *Psychiatry Clin. Neurosci.* **75**, 250–255 (2021).
93. S. Momtazmanesh, Z. Amirimoghaddam-Yazdi, H. S. Moghaddam, M. R. Mohammadi, S. Akhondzadeh, Sulforaphane as an adjunctive treatment for irritability in children with autism spectrum disorder: A randomized, double-blind, placebo-controlled clinical trial. *Psychiatry Clin. Neurosci.* **74**, 398–405 (2020).
94. A. W. Zimmerman, K. Singh, S. L. Connors, H. Liu, A. A. Panjwani, L. C. Lee, E. Diggins, A. Foley, S. Melnyk, I. N. Singh, S. J. James, R. E. Frye, J. W. Fahey, Randomized controlled trial of sulforaphane and metabolite discovery in children with Autism Spectrum Disorder. *Mol. Autism.* **12**, 38 (2021).
95. F. Dickerson, A. Origoni, E. Katsafanas, A. Squire, T. Newman, J. Fahey, J. C. Xiao, C. Stallings, J. Goga, S. Khushalani, R. Yolken, Randomized controlled trial of an adjunctive sulforaphane nutraceutical in schizophrenia. *Schizophr. Res.* **231**, 142–144 (2021).
96. T. W. Sedlak, L. G. Nucifora, M. Koga, L. S. Shaffer, C. Higgs, T. Tanaka, A. M. Wang, J. M. Coughlin, P. B. Barker, J. W. Fahey, A. Sawa, Sulforaphane augments glutathione and influences brain metabolites in human subjects: A clinical pilot study. *Mol. Neuropsychiatry* **3**, 214–222 (2018).
97. Y. Yagishita, T. N. Gatbonton-Schwager, M. L. McCallum, T. W. Kensler, Current landscape of NRF2 biomarkers in clinical trials. *Antioxidants (Basel)* **9**, 716 (2020).
98. A. Saito, S. Ishikawa, K. Yang, A. Sawa, K. Ishizuka, Sulforaphane as a potential therapeutic agent: A comprehensive analysis of clinical trials and mechanistic insights. *J. Nutr. Sci.* **14**, e65 (2025).
99. F. Schwenk, U. Baron, K. Rajewsky, A cre-transgenic mouse strain for the ubiquitous deletion of loxP-flanked gene segments including deletion in germ cells. *Nucleic Acids Res.* **23**, 5080–5081 (1995).
100. M. Paukert, A. Agarwal, J. Cha, V. A. Doze, J. U. Kang, D. E. Bergles, Norepinephrine controls astroglial responsiveness to local circuit activity. *Neuron* **82**, 1263–1270 (2014).
101. T. Mori, K. Tanaka, A. Buffo, W. Wurst, R. Kuhn, M. Gotz, Inducible gene deletion in astroglia and radial glia—A valuable tool for functional and lineage analysis. *Glia* **54**, 21–34 (2006).
102. C. Postic, M. Shiota, K. D. Niswender, T. L. Jetton, Y. Chen, J. M. Moates, K. D. Shelton, J. Lindner, A. D. Cherrington, M. A. Magnuson, Dual roles for glucokinase in glucose homeostasis as determined by liver and pancreatic β cell-specific gene knock-outs using Cre recombinase. *J. Biol. Chem.* **274**, 305–315 (1999).
103. M. R. Regan, Y. H. Huang, Y. S. Kim, M. I. Dykes-Hoberg, L. Jin, A. M. Watkins, D. E. Bergles, J. D. Rothstein, Variations in promoter activity reveal a differential expression and physiology of glutamate transporters by glia in the developing and mature CNS. *J. Neurosci.* **27**, 6607–6619 (2007).
104. A. Hayashi-Takagi, M. Takaki, N. Graziane, S. Seshadri, H. Murdoch, A. J. Dunlop, Y. Makino, A. J. Seshadri, K. Ishizuka, D. P. Srivastava, Z. Xie, J. M. Baraban, M. D. Houslay, T. Tomoda, N. J. Brandon, A. Kamiya, Z. Yan, P. Penzes, A. Sawa, Disrupted-in-Schizophrenia 1 (DISC1) regulates spines of the glutamate synapse via Rac1. *Nat. Neurosci.* **13**, 327–332 (2010).
105. A. W. Johnson, H. Jaaro-Peled, N. Shahani, T. W. Sedlak, S. Zoubovsky, D. Burruss, F. Emiliani, A. Sawa, M. Gallagher, Cognitive and motivational deficits together with prefrontal oxidative stress in a mouse model for neuropsychiatric illness. *Proc. Natl. Acad. Sci. U.S.A.* **110**, 12462–12467 (2013).

Downloaded from https://www.science.org on August 04, 2026

106. M. Niwa, A. Kamiya, R. Murai, K. Kubo, A. J. Gruber, K. Tomita, L. Lu, S. Tomisato, H. Jaaro-Peled, S. Seshadri, H. Hiyama, B. Huang, K. Kohda, Y. Noda, P. O'Donnell, K. Nakajima, A. Sawa, T. Nabeshima, Knockdown of DISC1 by in utero gene transfer disturbs postnatal dopaminergic maturation in the frontal cortex and leads to adult behavioral deficits. *Neuron* **65**, 480–489 (2010).
107. T. Hikida, H. Jaaro-Peled, S. Seshadri, K. Oishi, C. Hookway, S. Kong, D. Wu, R. Xue, M. Andrade, S. Tankou, S. Mori, M. Gallagher, K. Ishizuka, M. Pletnikov, S. Kida, A. Sawa, Dominant-negative DISC1 transgenic mice display schizophrenia-associated phenotypes detected by measures translatable to humans. *Proc. Natl. Acad. Sci. U.S.A.* **104**, 14501–14506 (2007).
108. Spacebar Clicker, SpaceBarClicker.org (2020), https://spacebarclicker.org/.
109. W. N. Frankel, Y. Yang, C. L. Mahaffey, B. J. Beyer, T. P. O'Brien, Szt2, a novel gene for seizure threshold in mice. *Genes Brain Behav.* **8**, 568–576 (2009).
110. Y. S. Bae, W. Chung, K. Han, K. Y. Park, H. Kim, E. Kim, M. H. Kim, Down-regulation of RalBP1 expression reduces seizure threshold and synaptic inhibition in mice. *Biochem. Biophys. Res. Commun.* **433**, 175–180 (2013).
111. S. Andrews, FastQC: A Quality Control Tool for High Throughput Sequence Data [Online] (2010).
112. A. Dobin, C. A. Davis, F. Schlesinger, J. Drenkow, C. Zaleski, S. Jha, P. Batut, M. Chaisson, T. R. Gingeras, STAR: Ultrafast universal RNA-seq aligner. *Bioinformatics* **29**, 15–21 (2013).
113. M. I. Love, W. Huber, S. Anders, Moderated estimation of fold change and dispersion for RNA-seq data with DESeq2. *Genome Biol.* **15**, 550 (2014).
114. A. Subramanian, P. Tamayo, V. K. Mootha, S. Mukherjee, B. L. Ebert, M. A. Gillette, A. Paulovich, S. L. Pomeroy, T. R. Golub, E. S. Lander, J. P. Mesirov, Gene set enrichment analysis: A knowledge-based approach for interpreting genome-wide expression profiles. *Proc. Natl. Acad. Sci. U.S.A.* **102**, 15545–15550 (2005).
115. M. You, M. Tian, Z. Song, Z. Liu, B. Yang, S. Zhang, Selection of GalNAc-conjugated siKeap1 as disease-specific delivery system for chemotherapy-induced liver injury and chronic liver disease. *Nano Lett.* **24**, 1096–1105 (2024).
116. Y. Fujikawa, L. P. Roma, M. C. Sobotta, A. J. Rose, M. B. Diaz, G. Locatelli, M. O. Breckwoldt, T. Misgeld, M. Kerschensteiner, S. Herzig, K. Muller-Decker, T. P. Dick, Mouse redox histology using genetically encoded probes. *Sci. Signal.* **9**, rs1 (2016).
117. Y. S. Zhang, K. L. Wade, T. Prestera, P. Talalay, Quantitative determination of isothiocyanates, dithiocarbamates, carbon disulfide, and related thiocarbonyl compounds by cyclocondensation with 1,2-benzenedithiol. *Anal. Biochem.* **239**, 160–167 (1996).
118. L. X. Ye, A. T. Dinkova-Kostova, K. L. Wade, Y. S. Zhang, T. A. Shapiro, P. Talalay, Quantitative determination of dithiocarbamates in human plasma, serum, erythrocytes and urine: Pharmacokinetics of broccoli sprout isothiocyanates in humans (vol 316, pg 43, 2002). *Clin. Chim. Acta* **321**, 127–129 (2002).
119. J. Drouin-Ouellet, A. L. Brownell, M. Saint-Pierre, C. Fasano, V. Emond, L. E. Trudeau, D. Levesque, F. Cicchetti, Neuroinflammation is associated with changes in glial mGluR5 expression and the development of neonatal excitotoxic lesions. *Glia* **59**, 188–199 (2011).
120. P. Zhou, S. L. Resendez, J. Rodriguez-Romaguera, J. C. Jimenez, S. Q. Neufeld, A. Giovannucci, J. Friedrich, E. A. Pnevmatikakis, G. D. Stuber, R. Hen, M. A. Kheirbek, B. L. Sabatini, R. E. Kass, L. Paninski, Efficient and accurate extraction of in vivo calcium signals from microendoscopic video data. *Elife* **7**, e28728 (2018).
121. E. A. Pnevmatikakis, D. Soudry, Y. Gao, T. A. Machado, J. Merel, D. Pfau, T. Reardon, Y. Mu, C. Lacefield, W. Yang, M. Ahrens, R. Bruno, T. M. Jessell, D. S. Peterka, R. Yuste, L. Paninski, Simultaneous denoising, deconvolution, and demixing of calcium imaging data. *Neuron* **89**, 285–299 (2016).
122. M. Murugan, H. J. Jang, M. Park, E. M. Miller, J. Cox, J. P. Taliaferro, N. F. Parker, V. Bhave, H. Hur, Y. Liang, A. R. Nectow, J. W. Pillow, I. B. Witten, Combined social and spatial coding in a descending projection from the prefrontal cortex. *Cell* **171**, 1663–1677.e16 (2017).
123. J. T. Ting, T. L. Daigle, Q. Chen, G. Feng, Acute brain slice methods for adult and aging animals: Application of targeted patch clamp analysis and optogenetics. *Methods Mol. Biol.* **1183**, 221–242 (2014).
124. J. A. Stogsdill, J. Ramirez, D. Liu, Y. H. Kim, K. T. Baldwin, E. Enustun, T. Ejikeme, R. R. Ji, C. Eroglu, Astrocytic neuroligins control astrocyte morphogenesis and synaptogenesis. *Nature* **551**, 192–197 (2017).
125. L. Chindelevitch, D. Ziemek, A. Enayetallah, R. Randhawa, B. Sidders, C. Brockel, E. S. Huang, Causal reasoning on biological networks: Interpreting transcriptional changes. *Bioinformatics* **28**, 1114–1121 (2012).
126. S. Oki, T. Ohta, G. Shioi, H. Hatanaka, O. Ogasawara, Y. Okuda, H. Kawaji, R. Nakaki, J. Sese, C. Meno, ChIP-Atlas: A data-mining suite powered by full integration of public ChIP-seq data. *EMBO Rep.* **19**, e46255 (2018).


**Acknowledgments:** We thank M. Papapavlou, S. Deshpande, H. Zhang, K. Wade, K. Stephenson, T. H. Tran, Y. Wang, and T. R. Sato for technical assistance, as well as M. Pletnikov, J. Rothstein, and H. Faust for helpful discussions. We also thank Y. Lema for assistance preparing the figures and H. West-Foyle for help with ImageJ macros used for $Ca^{2+}$ imaging analysis. We are grateful to J. Rothstein for providing *Slc1a2*$^{EGFP}$ mice, M. Götz for providing *Slc1a3*$^{CreER}$ mice, and C. Eroglu for sharing protocols and technical advice. Schematics were created with Biorender.com. **Funding:** This work was supported by the National Institutes of Health grant MH-107730 (A.Saw.), National Institutes of Health grant MH-105660 (A.Saw.), National Institutes of Health grant MH-094268 (A.Saw.), National Institutes of Health grant MH-136297 (A.Saw.), Stanley (A.Saw.), S-R/RUSK (A.Saw.), NARSAD (A.Saw.), Subsidies for Current Expenditures to Private Institutions of Higher Education from the Promotion and Mutual Aid Corporation for Private Schools of Japan (K.I.), National Institutes of Health grant NS050274 (Multiphoton Imaging Core), NIDA Intramural Research Program of the NIH (W.X.), NSF grant no. 1232825 (W.X.), NARSAD young investigator grant 24161 (A.A.), and Chica and Heinz Schaller Research Foundation grant (A.A.). **Author contributions:** Conceptualization: T.E.F., D.E.B., and A.Saw. Data curation: T.E.F., A.Sai., and K.Y. Formal analysis: TEF, A.Sai., S.I., K.Y., W.X., H.N., A.A., B.L., and K.I. Funding acquisition: A.Saw. Investigation: T.E.F., A.Sai., S.I., K.Y., W.X., H.N., A.A., A.R., B.L., L.H., R.S., S.A., S.S., T.P., T.C.-P., D.W., E.C., R.Y., J.W.F., H.J.-P., and K.I. Methodology: T.E.F., A.Sai., K.Y., A.A., D.E.B., and A.Saw. Project administration: A.Saw. Resources: T.E.F., A.Sai., A.A., J.W.F., D.E.B., and A.Saw. Supervision: D.E.B., K.I., and A.Saw. Validation: T.E.F., A.Sai., A.A., and K.I. Visualization: T.E.F., A.Sai., AA, and A.Saw. Writing—review and editing: T.E.F., A.Sai., K.Y., W.X., A.A., J.W.F., D.E.B., K.I., and A.Saw. Writing—original draft: T.E.F. and A.Saw. **Competing interests:** J.W.F. is a scientific advisor for companies that produce both food and supplements related to broccoli, broccoli sprouts, and broccoli seeds and hence to the phytochemical SFN (Brassica Protection Products, FoodNerd, The Sprouting Company, and PhytoSmart). The other authors declare that they have no competing interests. **Data, code, and materials availability:** The RNA-seq expression data are available at the NCBI Gene Expression Omnibus (GEO; https://ncbi.nlm.nih.gov/geo/) under accession numbers GSE328106 and GSE329414. The code used for DESeq2 and GSEA is available at GitHub (https://github.com/KunYang99/ALDH7A1) and archived at Zenodo (https://doi.org/10.5281/zenodo.20719402). The CasCaDe MATLAB code for analysis of microdomain $Ca^{2+}$ events was previously described and is freely available (*49*). Sequences for all newly generated plasmids are publicly available in GenBank (https://ncbi.nlm.nih.gov/genbank/) under accession numbers PZ285974, PZ285975, PZ285976, PZ285977, PZ285978, and PZ285979. All other data and code needed to evaluate and reproduce the results in the paper are present in the paper and/or the Supplementary Materials. The materials and reagents generated in this study can be provided by A.Saw. pending scientific review and a completed material transfer agreement through the Johns Hopkins University School of Medicine. Requests for the materials should be submitted to: asawa1@jhmi.edu.

Submitted 21 January 2026
Accepted 22 June 2026
Published 29 July 2026
10.1126/sciadv.aef6777

Downloaded from https://www.science.org on August 04, 2026

ScienceAdvances

# Astrocyte redox imbalance underlies prelimbic neuronal hypoactivity and maladaptive affective behaviors in epilepsy

Travis E. Faust, Atsushi Saito, Shoichi Ishikawa, Kun Yang, Wendy Xin, Ho Namkung, Amit Agarwal, Adriana Ramos, Brian J. Lee, Lindsay Hayes, Rupali Srivastava, Sunday Adelakun, Sneha Saha, Trexy Palen, Tyler Cash-Padgett, Daniel J. Wood, Elisa Carloni, Ryosuke Yusa, Hanna Jaaro-Peled, Jed W. Fahey, Dwight E. Bergles, Koko Ishizuka, and Akira Sawa

*Sci. Adv.* **12** (31), eaef6777. DOI: 10.1126/sciadv.aef6777

**View the article online**
https://www.science.org/doi/10.1126/sciadv.aef6777
**Permissions**
https://www.science.org/help/reprints-and-permissions

Downloaded from https://www.science.org on August 04, 2026

Use of this article is subject to the Terms of service

*Science Advances* (ISSN 2375-2548) is published by the American Association for the Advancement of Science. 1200 New York Avenue NW, Washington, DC 20005. The title *Science Advances* is a registered trademark of AAAS.

Copyright © 2026 The Authors, some rights reserved; exclusive licensee American Association for the Advancement of Science. No claim to original U.S. Government Works. Distributed under a Creative Commons Attribution License 4.0 (CC BY).